Forest Ecology and Management 424 (2018) 323–337

Contents lists available at ScienceDirect

Forest Ecology and Management

journal homepage: www.elsevier.com/locate/foreco

Estimating aboveground carbon density across forest landscapes of Hawaii: Combining FIA plot-derived estimates and airborne LiDAR

R. Flint Hughes[a,*], Gregory P. Asner[b], James A. Baldwin[e], Joseph Mascaro[c], Lori K.K. Bufil[d], David E. Knapp[b]

[a] Institute of Pacific Islands Forestry, Pacific Southwest Research Station, USDA Forest Service, Hilo, HI 96720, USA
[b] Department of Global Ecology, Carnegie Institution for Science, Stanford, CA 94305, USA
[c] Planet, San Francisco, CA 94103, USA
[d] Research Corporation of the University of Hawaii, Honolulu, HI 96848, USA
[e] Pacific Southwest Research Station, USDA Forest Service, Albany, CA 94710, USA

ARTICLE INFO

Keywords:
Forest carbon
Inventories
LiDAR
Hawai'i
Hawai'i Experimental Tropical Forest
Invasive species
Carnegie Airborne Observatory

ABSTRACT

Remote sensing data have increasingly been employed in combination with field plot data to estimate aboveground carbon (C) stocks across heterogeneous forested landscapes around the world. The Forest Inventory and Analysis (FIA) program of the US Forest Service offers a gridded network of field plots which potentially can be linked to airborne Light Detection and Ranging (LiDAR) data to estimate forest aboveground carbon density (ACD; units of Mg C ha^{-1}). Here we utilized FIA plot and airborne LiDAR data sets collected across two contrasting landscapes known as Laupahoehoe and Pu‘u Wa‘awa‘a on Hawai'i Island to explore strengths and weaknesses of linking those two data sets to estimate ACD. We varied FIA plot sample designs with respect to sampling density (i.e., the number of plots across landscape) and intensity (i.e., the structural detail within inventory plots) to test the capability of the mapping approach. Results indicated that Laupahoehoe and Pu‘u Wa‘awa‘a landscapes supported an estimated 545 Gg C and 157 Gg C aboveground, respectively, and mean ACD values of the wet windward Laupahoehoe landscape (109 Mg ha^{-1}) were an order of magnitude greater than those of the leeward dry Pu‘u Wa‘awa‘a landscape (9.7 Mg ha^{-1}). Patterns of ACD were largely determined by combined factors of precipitation, lava substrate, prior land use, and presence of non-native, often invasive, species. Results demonstrated the relative importance of sample plot density over sample plot intensity, and showed that FIA inventory plots, even at their lowest sample intensity design, can be linked with LiDAR data to accurately estimate ACD across spatially heterogeneous landscapes. We also developed and applied a straightforward, statistically-robust approach to provide error estimates for the 100 million pixels that characterize the Laupahoehoe and Pu‘u Wa‘awa‘a landscapes as well as for any sub-units of those landscapes. We contend that augmenting existing FIA forest plot data with airborne LiDAR coverage, even if that requires an increase in plot density somewhat above the FIA standard 1X or 2X approaches, is a feasible, cost-effective, scientifically sound approach from which to obtain accurate landscape- to regional-scale ACD measures across the extensive and heterogeneous forests of the United States.

1. Introduction

Forests contain 70 to 90% of earth's estimated 1300 Pg of terrestrial biomass (Houghton et al., 2009), the majority of which occurs aboveground (Cairns et al., 1997). As carbon (C) accounts for approximately 50% of biomass, changes in forests due to natural or anthropogenic disturbances (e.g., storms, drought, pathogens, harvesting, deforestation, agricultural conversion) or through forest growth have a profound influence on the global carbon balance. For example, recent deforestation in the tropics has resulted in estimated 1.5 Pg C per annum fluxes to the atmosphere, or 16% of total anthropogenic emissions (Canadell et al., 2007), and C sequestration via forest growth in the United States offset an estimated 14% of that nation's C emissions in 2010 (US Environmental Protection Agency, 2012). Widespread recognition of the importance that forests play in the global C cycle has resulted in international programs, such as UN-REDD+, which seek to mitigate greenhouse gas emissions through forest protection (UN-REDD, 2012). An underlying tenant of such programs is that monetary

* Corresponding author.
E-mail address: fhughes@fs.fed.us (R.F. Hughes).

https://doi.org/10.1016/j.foreco.2018.04.053
Received 19 January 2018; Received in revised form 25 April 2018; Accepted 27 April 2018

compensation for forest C sequestration be based on spatially explicit, not to mention accurate, accounting of C across often heterogeneous forest landscapes.

Although there is broad agreement regarding the need to accurately quantify forest C stocks and dynamics at regional, national, and global scales, doing so remains a challenge. To date, national forest inventory networks (NFI) have been used to provide forest carbon estimates (McRoberts, 2010); in the United States the Forest Inventory and Analysis (FIA) program of the US Forest Service has served this role (Domke et al., 2014). FIA employs a gridded network of field plots in which forest composition and structure are measured along with many additional parameters (Bechtold and Patterson, 2005) and from which aboveground biomass and C can be estimated at the individual tree- and plot-level (Chave et al., 2005). This program has provided useful information regarding such topics as forest productivity (Waring et al., 2014), timber harvest patterns (Belote and Aplet, 2014), species distributions and shifts in response to climate change (Desprez et al., 2014, Gibson et al., 2014), non-native plant invasions (Wang et al., 2011, Huebner et al., 2009,) and pest outbreaks (Thompson, 2009, Haavik et al., 2012). FIA data have also informed recent research addressing C storage and dynamics in U.S. forests (Blackard et al., 2008, Gray et al., 2014). Although the FIA plot network, when re-measured at regular intervals through time, can provide average aboveground forest C mass values and temporal changes of such values for given areas of interest (i.e., counties, forest types, land use designations), on its own it likely does not adequately address the spatial and temporal heterogeneity inherent across forested landscapes. Statistically, NFI programs including the FIA system are inherently limited to sampling, rather than producing wall-to-wall inventories, of aboveground forest C across broad regions.

Remote sensing in general, and large footprint LiDAR (light detection and ranging) in particular, has been employed in combination with field plot data to accurately estimate aboveground C across heterogeneous forested landscapes of the North America, Europe, South and Central America, Africa, and Polynesia (e.g., Lefsky et al., 1999, Drake et al., 2002, McRoberts et al., 2015). In most cases, these efforts have employed a plot-aggregate allometry approach in which sets of plot-based estimates of aboveground C density (ACD; units of $Mg\,C\,ha^{-1}$) are regressed against relevant LiDAR metrics from those same plot locations (e.g., mean canopy height for each given plot) to create models where the LiDAR metric and ACD value are the independent and dependent variables, respectively (Zolkos et al., 2013, Asner and Mascaro, 2014). In most cases, sampling plots used to estimate ACD have ranged from 0.1 ha to 1 ha in area, and all woody stems down to a relatively small diameter (e.g., ≥ 1 cm dbh, or ≥ 5 cm dbh) are measured across the entirety of the plot area (Zolkos et al., 2013, Asner and Mascaro, 2014).

Recently, FIA plot data have been combined with LiDAR data to estimate forest height, structure, and biomass across temperate landscapes of the United States, including Alaska (Skowronski et al., 2007, Walker et al., 2007, Kellndorfer et al., 2010, Chopping et al., 2011, Zhao et al., 2012). However, no studies have yet combined FIA and LiDAR data sets to estimate aboveground forest C mass across tropical landscapes. Nor have relationships between FIA plot data and LiDAR parameters been rigorously tested regarding the robustness of resulting C mass estimates and their attendant uncertainties. Previous studies on Hawai'i Island have inventoried aboveground C mass at landscape scales by combining airborne small footprint LiDAR data with non-FIA field plot estimates of aboveground C mass (Asner et al., 2009, Asner et al., 2011, Hughes et al., 2014). These non-FIA forest sampling plots have tended to be greater in area, and have measured woody stems in a more comprehensive manner relative to FIA plots (Asner et al., 2011). Given the recent installation of FIA plots across areas of Hawai'i Island where high resolution LiDAR data have been acquired previously (Asner et al., 2011), we now have the opportunity to explicitly evaluate the usefulness of FIA plot data in combination with LiDAR data to estimate aboveground forest C mass. Several questions arise regarding this approach. First, are sample areas of FIA plots sufficient in size to successfully integrate with LiDAR canopy parameters to predict aboveground C mass? If not, how much more area should be sampled to increase their utility? Second, does the FIA nested sampling approach, in combination with LiDAR canopy metrics, provide C mass estimates with low levels of uncertainty? If not, how should one alter sampling methods to make them more useful for this application? Third, what are the fewest number of FIA plots needed across a given landscape to develop useful relationships with LiDAR canopy metrics to predict aboveground C mass across that landscape?

Given the above questions, our objectives were to utilize recently acquired FIA plot and airborne LiDAR data sets collected within the boundaries of the Hawai'i Experimental Tropical Forest (HETF) to explore the strengths and weaknesses of using FIA plots to inform LiDAR metrics to estimate aboveground C mass across broad areas of LiDAR coverage. Specifically, we evaluated how differing levels of FIA plot sampling intensity (i.e., the manner in which aboveground C mass is measured on a given plot) and plot density (i.e., the number of plots across a landscape) used in combination with spatially explicit LiDAR data influence both the aboveground forest C mass values and the uncertainties associated with those values. We also wished to determine the effects of varying FIA plot intensity and density on aboveground forest C estimates and uncertainties when only FIA plots are used to estimate forest C mass at the landscape scale, rather than in combination with LiDAR data sets to estimate forest C mass.

2. Methods

2.1. Study area

We conducted this study across the Laupahoehoe and Pu'u Wa'awa'a regions of Hawai'i Island (Fig. 1), which constitute the wet windward and dry leeward units, respectively, of the Hawai'i Experimental Tropical Forest (HETF), part of the USDA Forest Service Experimental Forest and Range System. These areas are administered and managed by the state of Hawai'i's Department of Land and Natural Resources (DLNR); Laupahoehoe includes Forest Reserve and Natural Area Reserve management designations, and Pu'u Wa'awa'a includes Wildlife (Forest Bird) Sanctuary, Forest Reserve, and State Parks Reserve management designations. Together, both areas account for 20,726 ha.

The Laupahoehoe HETF unit occupies 4990 ha and ranges in elevation from ca. 700 m to 1900 m asl. Mean annual temperature (MAT) decreases from 20 °C at lower elevations to 12 °C at upper elevations (Sanderson, 1993); mean annual rainfall decreases from 4907 mm at lower elevations (i.e., 668 m) to 1980 mm at upper elevations (i.e., 1762 m) to (Table 1; Giambelluca et al., 2013). Soils originate from three distinct lava substrates emanating from Mauna Kea Volcano whose ages range from 4000 to 250,000 YBP (Wolfe and Morris, 1996).

The Pu'u Wa'awa'a HETF unit encompasses 15,706 ha and ranges in elevation from sea level to 1951 m asl. MAT decreases from 23 °C along the coast to 14 °C at upper elevations (Sanderson, 1993); mean annual rainfall increases from 266 mm along the coast to 703 mm at upper elevations (i.e., 1582 m) (Table 1; Giambelluca et al., 2013). Soils originate from lava substrates of 7 distinct flow age groups that emanated from Hualalai Volcano; flows range in age from CE 1790 or younger to 105,000 YBP (Wolfe and Morris, 1996).

Vegetation of Laupahoehoe varies with respect to elevation, hydrology, and native or non-native species dominance. The majority of the area has been characterized as closed forest co-dominated by Hawai'i's most common native tree species, *Metrosideros polymorpha* (ohia) and *Acaia koa* (koa) (Gon et al., 2006). Native forests at low elevations (i.e., 700–900 m) have been invaded by fast-growing, non-native species such as *Psidium cattleianum* (strawberry guava) and *Ficus rubiginosa* (banyan) (Asner et al., 2009). Upslope (i.e., 1400 to 1600 m

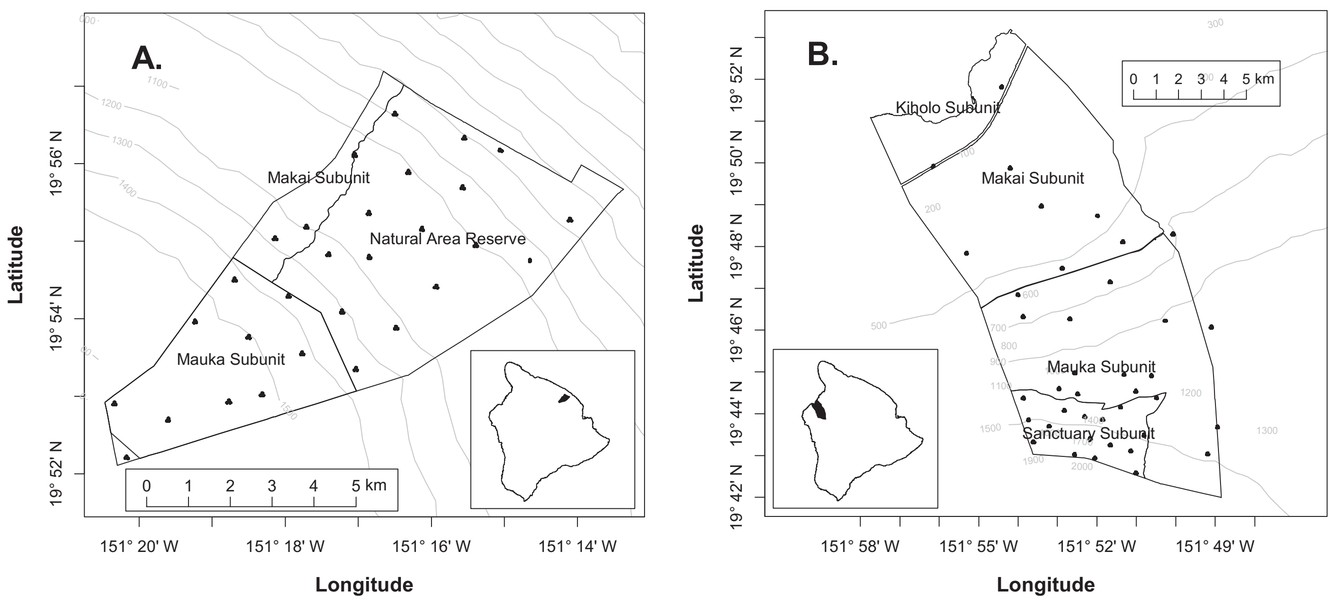

Fig. 1. Maps of the Laupahoehoe (A) and Pu‘u Wa‘awa‘a (B) units of the Hawai’i Tropical Experimental Forest located on Hawai’i Island, USA.

Table 1
Mean annual rainfall along elevation gradients of Laupahoehoe and Pu‘u Wa‘awa‘a units of the Hawaii Experimental Tropical Forest.

HETF Unit	Latitude	Longitude	Elevation (m)	Mean Annual Rainfall (mm)
Laupahoehoe	19.9480N	−155.2530W	668	4907
Laupahoehoe	19.9272N	−155.2674W	974	4167
Laupahoehoe	19.9091N	−155.2959W	1386	3156
Laupahoehoe	19.8862N	−155.3319W	1762	1980
Pu‘u Wa‘awa‘a	19.8548N	−155.9248W	1	266
Pu‘u Wa‘awa‘a	19.8129N	−155.8939W	363	435
Pu‘u Wa‘awa‘a	19.7670N	−155.8747W	835	683
Pu‘u Wa‘awa‘a	19.7281N	−155.8881W	1582	703

Source: Giambelluca et al. (2013).

a.s.l), mature stands of *Fraxinus uhdei* (tropical ash) extend across large areas; these were planted as part of the Civilian Conservation Corps (CCC) tree planting projects within Hawai’i’s Forest Reserves which peaked during the 1930’s (Woodcock, 2003). Open, mixed *A. koa* and *M. polymorpha* woodlands exhibiting continuous understory cover dominated by *Pennisetum clandestinum* (kikuyu grass) occur in the far upper reaches of Laupahoehoe. Poorly drained regions at mid-elevation support bog vegetation where stands of open-canopied, low stature *M. polymorpha* predominate.

Vegetation of the Pu‘u Wa‘awa‘a unit of HETF is a product of lava age, climate, non-native plant invasion, land use, and disturbance. Vegetation is largely absent from young lava flows of the area that are less than 214 years. Native vegetation on older flows along the coast and up to ca. 180 m a.s.l. has been largely replaced by dense to sparse stands of the non-native, phreatophytic tree, *Prosopis pallida* (Dudley et al., 2014). Ungulate grazing has led to reduced forest cover over large areas of mid- to upper elevations (Cuddihy and Stone, 1990), and non-native grasses such as *Pennisetum setaceum* (fountain grass) and *P. clandestinum* (kikuyu grass) (Blackmore and Vitousek, 2000) are well established in many of these areas, with the former dominating lower elevations and transitioning to the latter at upper elevations. Where such grasslands have burned over time, tree cover is further reduced. Open canopy *M. polymorpha* stands as well as closed canopy stands of the non-native tree, *Grevillia robusta* occur at mid-elevations (i.e., 900 to 1000 m). Extensive open and closed canopies co-dominated by *A. koa* and *M. polymorpha* occur within the fenced Forest Bird Sanctuary unit between 1280 and 1890 m a.s.l. (Gon et al., 2006).

2.2. Methodological approach

2.2.1. Plot selection and measurement

We selected plot locations in accordance with standard FIA basic grid plot criteria by overlaying a hexagonal grid over each unit and placing a single plot within each hexagon offset from the hex center by a random distance and azimuth (Bechtold and Patterson, 2005). The sampling design resulted in a total of 68 plots located across the two units of HETF; 28 plots were located in Laupahoehoe and 40 plots were located in Pu‘u Wa‘awa‘a. In terms of FIA sampling terminology, these plot frequencies approximated a 5× density for Pu‘u Wa‘awa‘a (i.e., plot per 420 ha), a 13× density for Laupahoehoe (i.e., one plot per 185 ha), and a 7× density for the combined areas (i.e., one plot per 392 ha) (Fig. 1). Although plots were relatively evenly distributed across nearly continuous forest cover of Laupahoehoe, plots were distributed less uniformly across Pu‘u Wa‘awa‘a. In the latter case plots were concentrated in areas of extant forest cover, particularly forest stands contained within the 1540 ha Forest Bird Sanctuary (Fig. 1).

Each forest plot consisted of four circular, 7.3 m radius subplots arranged in a tetrad-like design (Bechtold and Patterson, 2005) in which center points of subplots 2, 3, and 4 were spaced 36.6 m from the center of subplot 1 along azimuths of 360, 120 and 240°, respectively (Fig. 2). Each subplot was nested within a larger 17.9 m radius macroplot, and each subplot contained a smaller, 2.1 m radius microplot whose center was 3.7 m from each subplot center. As such, each subplot design encompassed 0.068 ha (i.e., sum of four 7.3 m radius sub-plots), and each macroplot design encompassed 0.4 ha (i.e., sum of four 17.9 m radius sub-plots). Genus and species, status (i.e., live or dead), and diameter at breast height (dbh; 1.4 m above the ground) were recorded for every tree exhibiting a dbh ≥ 12.7 cm present within each subplot and macroplot. Height (m) was measured and recorded for all trees with dbh values ≥ 12.7 cm in each subplot and for all trees with dbh values ≥ 61 cm at dbh in each macroplot. Genus, species, and dbh of all live saplings with dbh values ≥ 2.5 cm and < 12.7 cm were measured in each microplot located within each subplot. In all subsequent analyses, the four micro-, sub- , and macro-plots of each forest plot were treated as a single consolidated sample of that forest plot.

A GPS point was collected at the center of each subplot using a survey-grade Javad Maxor GGD (Javad Navigation Systems, Inc., Saratoga, CA, USA) placed in the center of each subplot and leveled atop a 1.8 m pole with bipod legs for stability. Once the receiver had obtained a signal from at least three American satellites and had solved

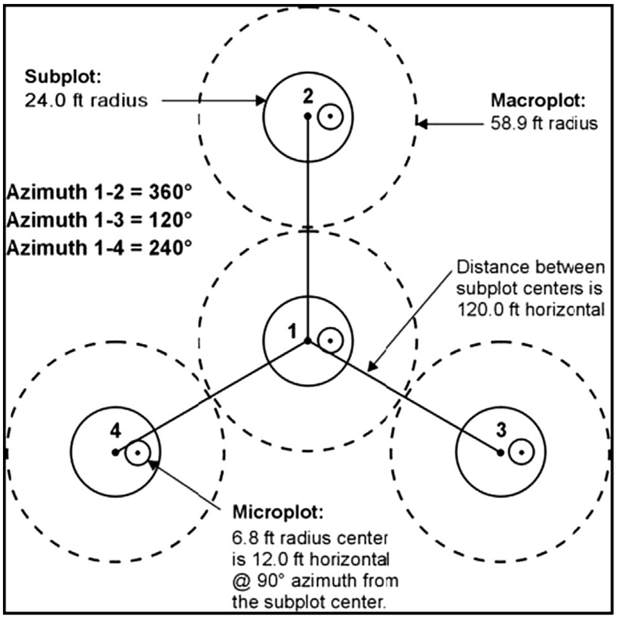

Fig. 2. Forest Inventory and Analysis plot design (Bechtold and Patterson, 2005).

a position, it recorded data for at least 30 min at a rate of 1 epoch/second. We used Javad Justin software and data from a continuously Operating Reference Station (National Geodetic Survey, NGS-NOAA) to perform post-processing differential corrections.

Our primary objective was to inventory – as opposed to sample – ACD in a "wall to wall" fashion across the Laupahoehoe and Pu'u Wa'awa'a units of the Hawai'i Experimental Tropical Forest. We did this by relating FIA plot-based estimates of ACD to forest canopy metrics derived from airborne LiDAR data. LiDAR data were acquired by the Carnegie Airborne Observatory (CAO) across a total of 20,726 ha of the two HETF units. LiDAR has the capacity to accurately detect various components of forest structure, including ground, subcanopy, and canopy layers at sub meter resolution (Lefsky et al., 2002). The CAO LiDAR was operated at 70 kHz, with a maximum half-scan angle of 17° (after a 2-degree cutoff) and 50% overlap between adjacent flight lines. The sensor-to-target range was maintained at 1000 m above ground level, with a standard deviation of < 100 m throughout data collection. LiDAR spot size at ground level ranged from 0.5 to 0.65 m from nadir to the edge of each scan line (17° off-nadir), with two laser shots (i.e., up to 8 returns) per location due to the adjacency of flight line overlap. Although Asner et al. (2011) and Hughes et al. (2014) previously compared landscapes using LiDAR-derived mean canopy profile height (MCH), here we employed top-of-canopy height (TCH); this was done because TCH is more generalized across sensor types (Gobakken and Næsset, 2009, Asner and Mascaro, 2014). TCH values, or vegetation height at 1.12 m resolution, constituted the difference of surface and terrain models (Asner et al., 2009). Laser ranges from the LiDAR data were ortho-rectified with embedded high resolution Global Positioning System-Inertial Measurement Unit (GPS-IMU) data to determine the 3-D locations of laser returns, producing a 'cloud' of LiDAR data (Asner and Mascaro, 2014). Final TCH maps were gridded at a 1.5 m^2 pixel resolution (i.e., ca. 72 million pixels) for Pu'u Wa'awa'a, and at a 1.25 m^2 pixel resolution (i.e., ca. 32 million pixels) across Laupahoehoe (Fig. 3).

In each forest inventory plot the average value of all TCH pixels contained within it determined mean plot TCH. For example, subplots and macro-plots in the Laupahoehoe unit that were 0.017 and 0.1 ha, respectively, contained to 134 and 805 TCH measurements or pixels, respectively. Owing to the slightly lower pixel resolution of the data gathered across Pu'u Wa'awa'a, subplots and macroplots of that unit contained 112 and 671 pixels, respectively.

2.2.2. Aboveground C mass calculations

Carbon mass of trees and saplings was calculated using allometric equations of Asner et al. (2011); species specific equations were employed for *A. koa*, *M. polymorpha*, *P. cattleianum*, and *F. uhdei*, as well as tree ferns (e.g., *Cibotium* spp.). When species-specific equations were not available for particular species, aboveground C mass was calculated using allometric models provided by Chave et al. (2005) that were stratified by climate (i.e., dry, moist, and wet forest types). We classified forest types of all forest plots established in Laupahoehoe and Pu'u Wa'awa'a using mean annual rainfall values (Giambelluca et al., 2013); dry forest MAP was < 1500 mm, moist forest MAP was 1500 to 3500 mm, and wet forest MAP was > 3500 mm. Where equations from Chave et al. (2004) were employed, the independent variables dbh (cm^2), wood density (g cm^{-3}), and height (m) were used to predict aboveground C mass (Mg ha^{-1}). Tree specific dbh values were employed throughout. Species-specific wood density values (Asner et al., 2011) were employed where possible. If species-specific values were unavailable, we used genera-specific values. If genera-specific values were unavailable, we used a default value of 0.50 g cm^{-3}. Where actual tree heights were measured (i.e., for all trees on subplots and microplots, and trees with diameters ≥61 cm on macroplots), those values were employed; where actual tree height were not measured (i.e., for trees with diameters between 12.7 and 60.9 cm on macroplots), height was estimated from species-specific models relating height to diameter (Asner et al., 2011). In rare cases where species-specific height/diameter models were unavailable for a given species, models from Chave et al. (2005) which used diameter and wood density alone were used.

2.2.3. Statistical approach

We used regression models to predict aboveground C mass per unit area (Mg/ha) and C mass for the entirety of both Laupahoehoe and Pu'u Wa'awa'a landscapes; models determined the relationship between C mass estimates derived from FIA plots at discreet, known locations and mean LiDAR pixel heights that covered the same locations as each respective FIA forest plot (n = 68). Based on prior experience (Asner and Mascaro, 2014), we opted for an equation that allowed for increasing variability with increasing height in the following manner:

$$y = a\overline{ht}^b + \overline{ht}^k\varepsilon$$

where y is the estimated biomass per unit area in an FIA plot; $\overline{ht}$ is the mean height (i.e., TCH) from the associated pixels covering the given FIA plot; a, b, and k are constants to be estimated; and the residual error, ε, having a normal distribution with variance σ^2, ($\varepsilon \sim N(0, \sigma^2)$) (Asner and Mascaro, 2014).

The biomass estimate for any particular pixel where x is the associated TCH is constructed from estimates of a and b which are labeled as a and b: $\mu = ax^b$. Using the notation in McRoberts (2010) for the collection of N pixels in any given area of our overall study region in which we want to estimate aboveground C mass, we use a model-based estimate of mean C mass value per unit area (i.e., Mg ha^{-1}) calculated by the following:

$$\mu_{MOD} = \frac{1}{N}\sum_{i=1}^{N}\mu_i = \frac{1}{N}\sum_{i=1}^{N}ax_i^b$$

The estimate of variance around the mean C mass was calculated by the following (McRoberts, 2010):

$$\widehat{\mathrm{Var}}(\mu_{MOD}) = \frac{1}{N^2}\sum_{i=1}^{N}\sum_{j=1}^{N}\widehat{\mathrm{Cov}}(\mu_i, \mu_j)$$

where $\widehat{\mathrm{Cov}}(\mu_i, \mu_j)$ is the estimate of the covariance between the two estimators, μ_i and μ_j. Rather than use a subset of the N^2 estimates as McRoberts (2010) found necessary to make the calculation feasible, we applied some basic algebra to be able to use all N^2 covariances (Appendix A).

Primary among our objectives, we wished to evaluate the sensitivity

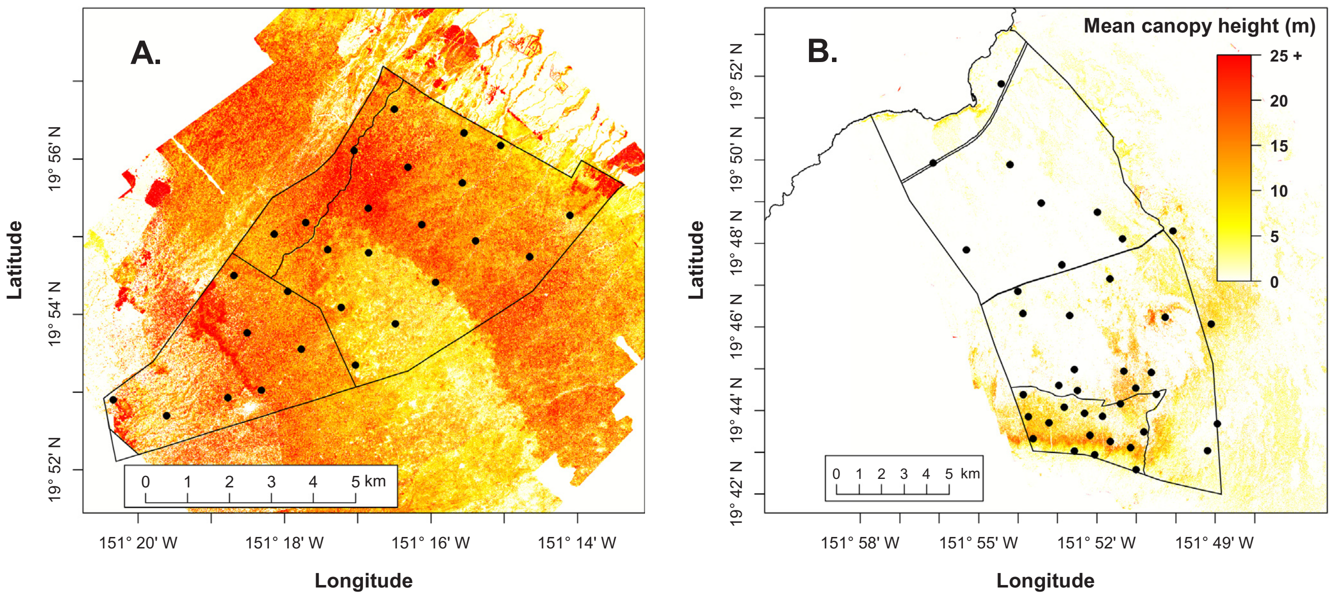

Fig. 3. Map of LiDAR-derived canopy height (m) across the Laupahoehoe (A) and Puʻu Waʻawaʻa (B) units of the Hawaiʻi Experimental Tropical Forest (HETF).

of aboveground forest C mass estimates to both plot sampling intensity (i.e., which forest components are measured, to what degree, and over what area in a given plot) and plot density (i.e., the number of plots arrayed across the area of interest). To address the influence of plot level sampling intensity on LiDAR based C mass estimates, we designated three distinct sampling degrees: (1) low intensity, in which all trees with dbh ≥ 12.7 cm were measured within each 7.3 m radius subplot; (2) medium intensity, in which all trees with dbh ≥ 12.7 cm were measured within each subplot and all trees with dbh values ≥ 61 cm were measured in each 17.9 m radius macroplot; (3) high intensity, in which all trees with dbh ≥ 12.7 cm were measured in the entirety of each macroplot. Saplings and small trees with dbh values ≥ 2.5 cm and < 12.7 cm were measured in each 2.1 m radius microplot for all three levels of sampling intensity.

We evaluated the sensitivity of forest C mass estimates to plot density by increasing, in a stepwise fashion, the number of plots used to generate TCH-to-C mass regression equations from a minimum of 10 plots to a maximum of 68 plots. We used a bootstrap approach (Efron, 1982) to select mean forest C mass values and their associated standard errors across this gradient of increasing plot density. We evaluated each of the three levels of sampling intensity (i.e., low intensity or sub-plot design, medium intensity or sub-plot + macro-plot design, and high intensity or enhanced macro-plot design) along these gradients of increasing plot density to simultaneously evaluate the relative sensitivities of forest C mass estimates to both sampling intensity and plot density.

We utilized a bootstrap approach to generate mean C mass values and their associated standard errors (Efron, 1982) for all combinations of sampling intensity and plot density. For any particular plot density/sampling intensity combination, we randomly sampled the respective number of plots from the total population of plots from which we generated equations and slopes relating TCH to C mass. We conducted 1000 iterations of this process, and applied each of those resulting 1000 regression equations to the pixels of Laupahoehoe, Puʻu Waʻawaʻa, and the total pixels of those two regions combined. Mean aboveground C mass values and their associated standard errors were obtained from the 1000 landscape scale applications of the equations for Laupahoehoe and Puʻu Waʻawaʻa.

In order to evaluate the potential increased accuracy gained from our FIA plot/LiDAR data approach relative to approaches using FIA plot data alone, we calculated landscape-scale mean ACD and associated standard error values for each of the various sampling intensities solely using data from the FIA plots. That is, we did not apply relationships between FIA plot-derived C mass and LiDAR-derived mean canopy height values to calculate ACD across the LiDAR coverages. We restricted this approach to the 28 FIA plots associated with the Laupahoehoe unit of the HETF because these plots were uniformly distributed across the Laupahoehoe unit landscape and thus represented an appropriate "sampling" of the Laupahoehoe unit. This was not the case for the Puʻu Waʻawaʻa unit where field plots were concentrated in upper, forested portions of the area. We calculated mean and standard error values for FIA plots within the Laupahoehoe unit for each of the 6 sampling intensity scenarios, and we estimated the precision obtained from using a different number of plots using the following approximation of the coefficient of variation for n plots:

$$cv_n \approx cv_{28}\sqrt{\frac{28}{n}}$$

This was equivalent to the common rule of thumb that assumes the standard error for n plots will be the standard deviation divided by the square root of the sample size, which can be rewritten in terms of sample size (n):

$$n \approx \frac{28 \times cv_{28}^2}{cv_n^2}$$

Using the above relationship, we estimated the sample size required to achieve a particular coefficient of variation (cv_n) for both the LiDAR assisted data approach and the "FIA plot data-only" approach.

3. Results

Based on models that employed the high intensity sampling regime (i.e., all trees with dbh ≥ 12.7 cm measured in the entirety of each 17.9 m-radius macroplot) and the highest plot density scenario (i.e., all 68 available plots), ACD across the total study area sampled was 702 Gg, with Laupahoehoe and Puʻu Waʻawaʻa units accounting for 545 Gg and 157 Gg of that total, respectively (Table 2). The Laupahoehoe unit, which is ca. 5000 ha in size, supported substantially more aboveground C than the much larger area of Puʻu Waʻawaʻa (ca. 16,000 ha). Averaged across each study unit, mean ACD values of the wet, windward side Laupahoehoe unit (109 Mg ha^{-1}) were over 10 times greater than those of the leeward, dry side Puʻu Waʻawaʻa unit (9.7 Mg ha^{-1}) (Table 2).

Table 2
Aboveground forest C mass (total and mean ± 1 SE) of the Laupahoehoe and Pu'u Wa'awa'a units and their respective subunits.

HETF Unit	Subunit	Area (ha)	Total Live C mass (Gg)	Mean Live C mass (Mg ha^{-1})	Total Live & Dead C mass (Gg)	Mean Live & Dead C mass (Mg ha^{-1})	Relative SE (%) Live	Relative SE (%) Live + Dead
Laupahoehoe	All	4994	545 ± 33	109.1 ± 6.7	564 ± 35	112.9 ± 7.0	6	6
Laupahoehoe	Makai	437	59 ± 4	135.1 ± 8.6	60 ± 4	138.4 ± 9.0	6	7
Laupahoehoe	Natural Area Res.	3059	327 ± 20	107.0 ± 6.4	340 ± 21	111.1 ± 6.8	6	6
Laupahoehoe	Mauka	1520	161 ± 10	105.7 ± 6.5	166 ± 10	109.0 ± 6.9	6	6
Pu'u Wa'awa'a	All	16,288	157 ± 8	9.7 ± 0.5	172 ± 9	10.6 ± 0.5	5	5
Pu'u Wa'awa'a	Kiholo	1447	5 ± 0	3.4 ± 0.2	6 ± 0	4.0 ± 0.2	5	6
Pu'u Wa'awa'a	Makai	6631	10 ± 1	1.6 ± 0.1	12 ± 1	1.8 ± 0.1	5	6
Pu'u Wa'awa'a	Mauka	6527	74 ± 4	11.4 ± 0.6	82 ± 4	12.5 ± 0.6	5	5
Pu'u Wa'awa'a	Bird Sanctuary	1572	68 ± 4	42.9 ± 2.3	73 ± 4	46.3 ± 2.5	5	5

Note: Relative SE values denote the percentage of a given mean value represented by its associated SE.
Mean C is expressed in megagrams (Mg) or 1×10^6 g. Total C is expressed in gigagrams (Gg) or 1×10^9 g.
Values are based on models that employed the enhanced plot sampling regime (i.e., all trees with dbh ≥ 12.7 cm measured over the entirety of each 17.9 m radius macroplot) and the highest plot density scenario (i.e., all 68 available plots).

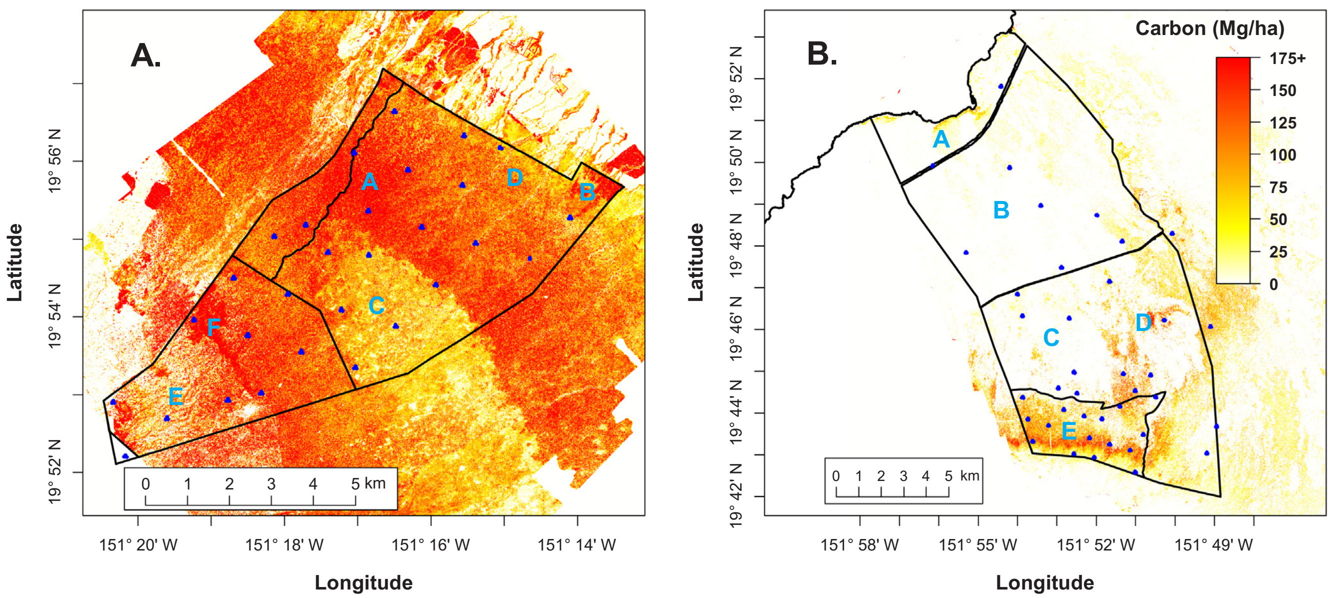

Fig. 4. Map of C aboveground mass (Mg ha^{-1}) across Laupahoehoe (A) and Pu'u Wa'awa'a (B) units of the HETF determined from landscape-scale LiDAR height (m) data and allometric relationships between mean canopy height and aboveground C (Mg/ha) of associated plots.

Considering the three subunits of Laupahoehoe, mean ACD ranged from 105 and 107 Mg ha^{-1} in the Mauka and Natural Area Reserve (NAR) subunits, respectively, to 135 Mg ha^{-1} in the Makai subunit (Fig. 4A, Table 2). Relatively high ACD values in the Makai subunit were due to the nearly continuous coverage of large *M. polymorpha*- and *A. koa*-dominated forest stands. Lower mean ACD values exhibited across the NAR subunit of Laupahoehoe resulted from a counterbalance of extensive stands of mature, high carbon, *M. polymorpha*-dominated forest at mid-elevations (205 Mg ha^{-1}; "A" in Fig. 4A), less extensive areas of large, planted *Eucalyptus* spp. stands at lower elevations (266 Mg ha^{-1}; "B" in Fig. 4A), a very large, water-saturated bog area at mid elevations exhibiting low ACD values (i.e., 58 Mg ha^{-1}; "C" in Fig. 4A), and low elevations heavily invaded by the small stature tree, *Psidium cattleianum* (76 Mg ha^{-1}; "D" in Fig. 4A). The Mauka subunit consisted of a mix of open *A. koa* and *M. polymorpha* co-dominated forest exhibiting relatively low ACD values (61 Mg ha^{-1}; "E" in Fig. 4A), stands of planted *Fraxinus uhdei* exhibiting high ACD (195 Mg ha^{-1}; "F" in Fig. 4A), and closed *A. koa* and *M. polymorpha* forest stand exhibiting values intermediate between the other two forest types.

Considering the four subunits of Pu'u Wa'awa'a, ACD ranged from 1.6 Mg ha^{-1} to 43 Mg ha^{-1} in the Makai and Bird Sanctuary subunits, respectively (Table 2, Fig. 4B). Although ACD averaged only 3.4 Mg ha^{-1} across the Kiholo subunit, relatively large stands of *Prosopis pallida* clustered along brackish water coastal margins exhibited values as high as 23 Mg ha^{-1} ("A" in Fig. 4B). Exceedingly low ACD values in the Makai subunit resulted from a paucity of woody vegetation and dominance of non-native grasses, particularly *Pennisetum setaceum,* throughout the majority of the area ("B" in Fig. 4B). ACD in the Mauka subunit ranged from < 5 Mg ha^{-1} in introduced grasslands of *P. setaceum* and *Pennisetum clandestinum* ("C" in Fig. 4B) to 86 Mg ha^{-1} in forest stands dominated by the non-native tree, *Grevillea robusta* ("D" in Fig. 4B).

Forests co-dominated by *A. koa* and *M. polymorpha* trees accounted for relatively high ACD values in the Bird Sanctuary subunit; the uppermost band of closed forest dominated by these two native tree species exhibited ACD values as high as 100 Mg ha^{-1} ("E" in Fig. 4B) (Table 2, Fig. 4B).

Relationships between LiDAR-derived canopy height and plot-derived C mass estimates were more strongly influenced by plot density (i.e., the number of plots used to create the relationship), than by sampling intensity (i.e., the degree to which C mass on a given plot was measured). Where plot density was constrained to approximate the standard FIA "1X" plot density regime (i.e., 1 plot for every ≈2400 ha),

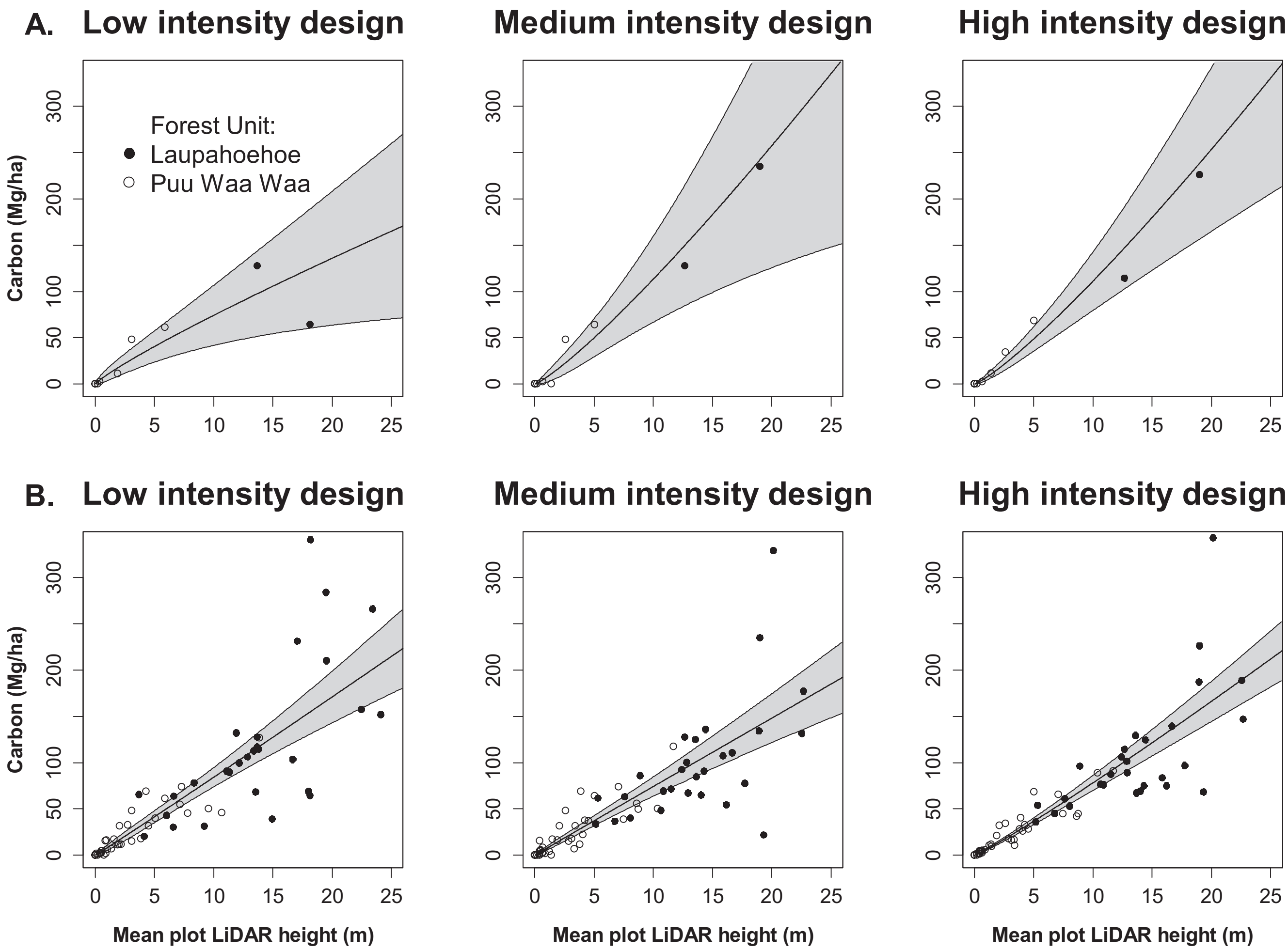

Fig. 5. Relationships between mean plot LiDAR height (m) and aboveground C (Mg/ha) for the combined Laupahoehoe and Pu‘u Wa‘awa‘a units of the Hawai’i Experimental Tropical Forest at 3 different plot sampling intensities (i.e., low, medium, and high) and at low (A) and high (B) plot densities (i.e., 1 plot per 2400 ha and 1 plot per 313 ha, respectively).

relationships between LiDAR canopy height and C mass provided poor ACD estimates regardless of sampling intensity; slopes of each of the three sampling intensity scenarios differed from each other, and variances of all three were uniformly high leading to low precision in estimation in each case (Fig. 5).

In contrast, maximum plot density trials in which all FIA plots sampled were employed (i.e., 68 plots, or 1 plot for every ≈313 ha) relationships between canopy height and C mass provided satisfactory estimates regardless of sampling intensity; that is, slopes were similar among the three sample intensities, and variances were uniformly low, leading to high precision of resulting estimates from relationships in each case (Fig. 5).

Bootstrap analysis demonstrated the importance of sample plot density on precision of C mass estimates at landscape scales (Fig. 6). Mean C mass estimates for the three sampling intensities averaged between 105 and 130 Mg ha^{-1} across the Laupahoehoe unit, between 10 and 12 Mg ha^{-1} across the Pu‘u Wa‘awa‘a unit, and between 33 and 40 Mg ha^{-1} across their combined landscapes (Fig. 6). Mean C mass estimates for each of the three areas were marginally greater for the low intensity design than the high intensity plot design, which were marginally greater than the medium intensity design (Fig. 6). In all cases, mean values remained highly stable across the plot density gradient; this resulted from our approach that averaged a thousand sampling iterations in each case. Standard error (SE) values, which here provide measures of how precisely the mean was estimated, were highest at low plot density (e.g., 20 plots used in Canopy Height/C mass regression models) for all three landscapes (Fig. 6). Values were generally higher for the medium intensity design than those of the low intensity design which were generally higher than those of the high intensity plot design. This was likely due to the relatively greater influence of very large trees in the medium intensity design where only trees ≥61 cm dbh were recorded in the macroplot area; in cases where large trees are encountered, they increase overall C mass greatly, particularly relative to plots that happen not to contain large trees in the macroplot sampling space. Within each landscape, SE values of the three sample intensities declined steeply as plot densities increased from 20 plots to 40 plots, after which SE values remained uniformly stable, approaching respective mean C mass estimates in an asymptotic manner (Fig. 6).

At low plot densities, relative standard errors (i.e., SE value divided by mean value) were relatively high and variable among the three sampling intensity scenarios. Considering the Laupahoehoe unit by itself, high, medium, and low sampling intensities were 20%, 23% and 40% of mean C mass values, respectively, at low plot densities (i.e., 20 plots) (Fig. 7B). Standard error values across Pu‘u Wa‘awa‘a at low densities were ca. 20%, 14%, and 12% of mean values for medium, low, and high plot intensities, respectively (Fig. 7C). Relative SE values for combined Lauphahoehoe and Pu‘u Wa‘awa‘a landscapes exhibited a similar pattern at low densities: values of high and low sampling intensities were ca. 13% of the mean, while the medium intensity sampling values were 25% of the mean. Between plot density values of 20 to 40 plots, relative SE values were highest for the medium sampling intensity, lowest for the high intensity, and intermediate for the low

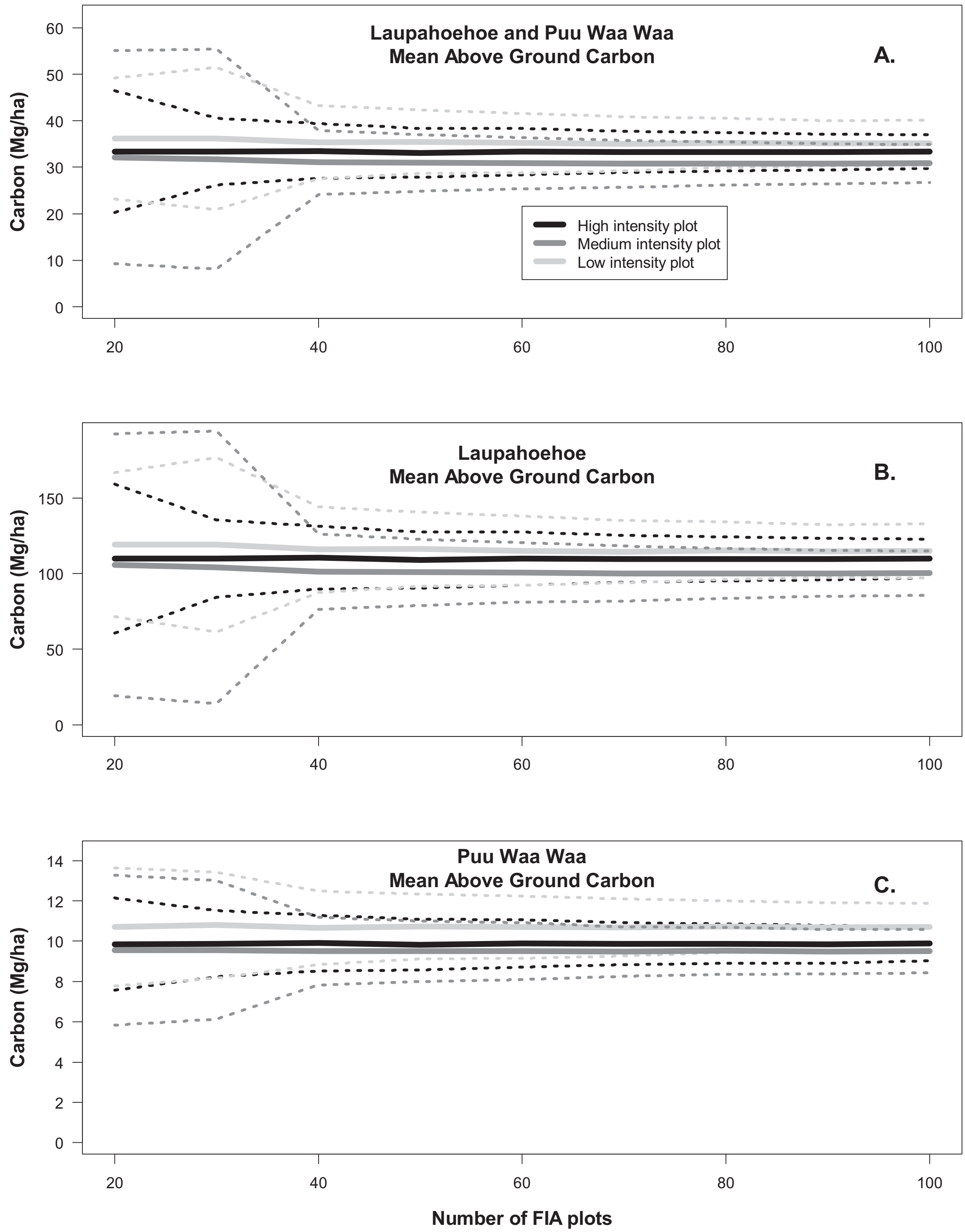

Fig. 6. Relationship between mean aboveground C mass (Mg ha^{-1}) and sampling density (i.e., number of plots used in the analysis) for combined Laupahoehoe and Pu'u Wa'awa'a landscapes (A), Laupahoehoe landscapes only (B), and Pu'u Wa'awa'a landscapes only (C). We used a bootstrap approach in which the particular numbers of plots were randomly sampled from the total population of plots from which equations and slopes relating TCH to C mass were generated. A total of 1000 iterations were conducted for each increase in plot number (i.e., from 20 to 100 plots); hence the observed stability of mean C mass values despite high variances around mean values at low plot densities. In all cases, dashed lines indicate standard error values.

intensity (Fig. 7). Once sampling densities surpassed 40 plots, relative S.E. values were low, convergent among each other, and very stable for each of the three areas of interest, regardless of sampling intensity scenario (Fig. 7). Values converged to ca. 10%, 7%, and 5% of mean values for Laupahoehoe, combined, and Pu'u Wa'awa'a landscapes, respectively (Fig. 7). Relative SE values of means for the total number of field plots in the study – 68 – were uniformly low (i.e., between 5 and 7% of the mean) for all sampling intensities and areas of interest (Fig. 7, Table 2).

Results from analyses that employed only FIA plot data to determine landscape-scale ACD for the Laupahoehoe unit indicated that, although mean values were similar to those of the LiDAR assisted approach, SE values and coefficients of variation were higher for the former approach compared to the latter (Table 3). Mean and SE values derived from data

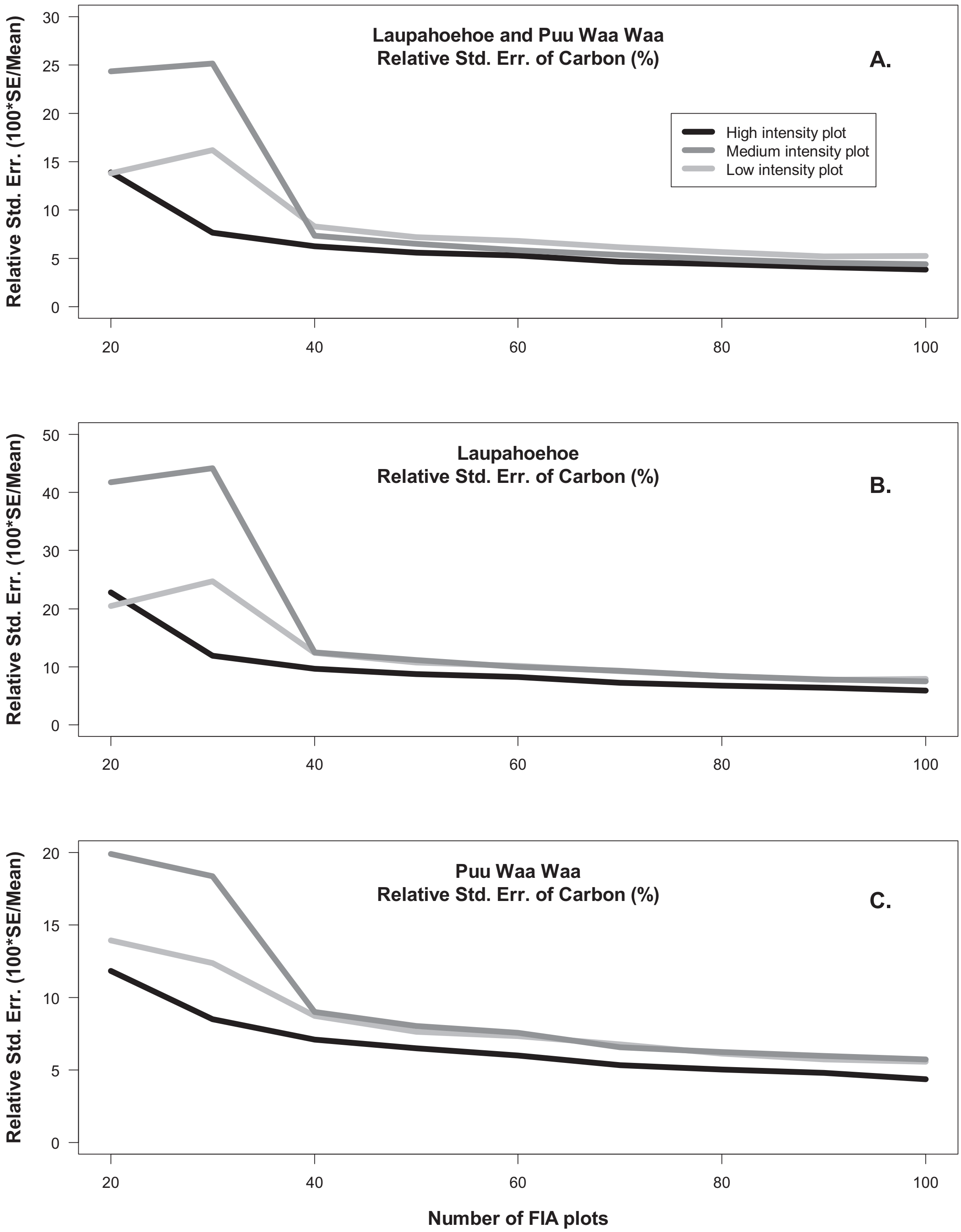

Fig. 7. Relationship between relative standard error values (i.e., SE/mean * 100) and number of plots used in the analysis at low, medium, and high sampling intensities across combined Laupahoehoe and Pu‘u Wa‘awa‘a landscapes (A), Laupahoehoe landscapes only (B), and Pu‘u Wa‘awa‘a landscapes only (C). We used a bootstrap approach in which the particular groups of plots were randomly sampled from the total population of plots from which equations and slopes relating TCH to C mass were generated. A total of 1000 iterations were conducted for each increase in plot number (i.e., from 20 to 100 plots).

of the 28 FIA plots located in Laupahoehoe (i.e., one forest plot per 180 ha) were calculated for both live biomass and combined live and dead (i.e., snags) biomass under the three sampling intensities (i.e., low, medium, and high intensity approaches). Coefficients of variation (CV) ranged from 10% to 13% of mean values that solely utilize the FIA plot data. In contrast, LiDAR-assisted approaches reduced the range of CV values to 6 to 8% (Table 3).

In addition, results indicated that under the constrained FIA-plot scenario sample sizes (n) required to reduce coefficients of variation (CV) to levels comparable to CV values of the LiDAR-assisted approach (i.e., precision of 6% to 8% of C mass mean values) would need to be 2- to 4-fold greater than the LiDAR-assisted values. This would necessitate installation of between 64 and 97 plots in the Laupahoehoe Forest Unit alone, compared to the density of 28 plots utilized in the LiDAR-assisted approach.

Table 3
Sample plot number, C mass (mean ± S.E.) and coefficients of variation (C.V.) estimates across the Laupahoehoe unit where plots are solely used to estimate C mass and C.V. estimates where LiDAR data is employed to estimate C mass.

Sampling Intensity	# of plots (n)	C mass (Mg ha^{-1}) without LiDAR	C.V. without LiDAR (%)	C.V. with LiDAR (%)	Plot # needed to equal LiDAR C.V.
Low Intensity (live trees)	28	118 ± 15	13	7	89
Medium Intensity (live trees)	28	99 ± 12	12	8	64
High Intensity (live trees)	28	108 ± 12	11	6	97
Low Intensity (live & dead trees)	28	137 ± 16	12	7	88
Medium Intensity (live & dead trees)	28	116 ± 12	10	7	65
High Intensity (live & dead trees)	28	115 ± 12	10	6	72

Note: The column titled "Plot # needed to equal LiDAR C.V." denotes the sample number required by the "FIA plot alone" approach to attain coefficient of variance values equivalent to those produced by the "FIA/LiDAR combined data" approach for each sample intensity scenario.

4. Discussion

Results document both the large aboveground C pools contained collectively within vegetation of the Laupahoehoe and Puʻu Waʻawaʻa landscapes – particularly in Laupahoehoe – and the wide variation in C density across those landscapes. High mean ACD values in Laupahoehoe were mainly due to the presence of extensive, large-stature forests dominated by native tree species, *M. polymorpha* and *A. koa*. Although *M. polymorpha* individuals tend not to grow remarkably tall relative to other tropical or subtropical species, the wood of this species is dense (i.e., 0.7 g/cm^3) and stand-level densities (i.e., stems ha^{-1}) of mature *M. polymorpha* forest are often quite high (e.g., 260 stems > 20 cm dbh ha^{-1}) (Zimmerman et al., 2008). Combined, these tree- and stand-level characteristics result in high ACD values where mature *M. polymorpha* forests dominate. *M. polymorpha* and *A. koa* are also primary contributors to portions of Puʻu Waʻawaʻa exhibiting high ACD values (Gon et al., 2006). Both relatively tall trees, *A. koa*, and *M. polymorpha* are the only two native trees that occupy intermediate-stature and emergent tree layers of Hawaiʻi's native forests. As such, these two dominant tree species account for the majority of native species contributions to ACD across Laupahoehoe and Puʻu Waʻawaʻa landscapes.

On average, ACD values in the moist to wet forests of Laupahoehoe (i.e., 105–135 Mg C ha^{-1}) were comparable to those of tropical forests found elsewhere. Humid forests of Madagascar and the Columbian Amazon exhibited average ACD values of 100 and 130 Mg C ha^{-1}, respectively (Asner et al., 2012a, Asner et al., 2012b), and forests of the Peruvian Amazon exhibited values ranging from 65 to 125 Mg C ha^{-1} (Asner et al., 2010). ACD across the Puʻu Waʻawaʻa landscape, ranging from 2 Mg ha^{-1} in non-native grasslands to 43 Mg ha^{-1} in montane mesic forests, was comparable to similar vegetation types in Hawaiʻi, Mexico, and the Amazon Basin (Litton et al., 2006, Navar, 2009, Saatchi et al., 2007).

The most striking pattern regarding environmental controls on ACD between Laupahoehoe and Puʻu Waʻawaʻa landscapes resulted from differences in precipitation. The range in mean annual rainfall values for Laupahoehoe (i.e., 1980 mm to 4907 mm) were an order of magnitude greater than those of Puʻu Waʻawaʻa (i.e., 266 to 703 mm); similarly, mean ACD for Laupahoehoe (i.e., 109 Mg ha^{-1}) was an order of magnitude greater than that of Puʻu Waʻawaʻa (i.e., 9.7 Mg ha^{-1}). Aplet et al. (1998) found aboveground biomass strongly and positively correlated with precipitation along a matrix of lava flows on windward and leeward slopes of Mauna Loa, Hawaiʻi. Previous studies have documented strong positive relationships between precipitation and ACD in India (Mehta et al., 2014), South America (Alvarez-Davila et al., 2017), and the Rocky Mountains of Colorado, U.S.A. (Swetnam et al., 2017).

Across both Laupahoehoe and Puʻu Waʻawaʻa landscapes, non-native species exerted a strong influence on patterns of ACD. Invasive, non-native grasses, particularly *Pennisetum setaceum* (fountain grass) and *P. clandestinum*, occupy large portions of Puʻu Waʻawaʻa (Blackmore and Vitousek, 2000) and, to a lesser extent, Laupahoehoe landscapes. They are responsible for generally low ACD values where they occur. Once grasses become established, typically in concert with ungulate activity (Leopold and Hess, 2017), they displace native woody species by increasing the intensity, frequency, and extent of fires (Trauernicht et al., 2015). Similar to invasive non-native grasses across Puʻu Waʻawaʻa, the small stature, non-native tree, *Psidium cattleianum* was ubiquitous across much of the lower portions of Laupahoehoe; where *P. cattleianum* occurred, ACD values were typically lower relative to adjacent *M. polymorpha* and *A. koa* dominated forest stands. Asner et al. (2009) documented a diminution in ACD across areas of *P. cattleianum* invasion. In contrast, non-native trees, *Fraxinus uhdei* and *Grevillea robusta,* increased ACD levels compared to native-dominated forests where they occurred. *F. uhdei* is fast growing, attains heights up to 40 m (Wagner et al., 1999), and grows in relatively dense stands. Similar to *F. uhdei*, *G. robusta* is a large tree, attaining heights of 10 to 25 m (Wagner et al., 1999). *G. robusta* ACD values were substantially higher than those of surrounding alien grasslands and comparable to ACD of adjacent mixed stands of *M. polymorpha* and *A. koa.*

Taken together, the landscapes of Laupahoehoe and Puʻu Waʻawaʻa represent a meso-cosm for most of the patterns of aboveground C density and the factors shaping them across the Hawaiian Islands. ACD of native plant communities are often heavily influenced – either positively or negatively – by non-native species invasions, and ACD values of both native and non-native dominated communities are strongly shaped by the influences of climate, land-use, and fire. Similar to results here, prior studies documented the important influences of precipitation, elevation, non-native species introductions, deforestation, fire, and grazing on ACD across Hawaiʻi (Asner et al., 2016). These landscape- scale findings agree with numerous prior plot-scale studies conducted in a variety of Hawaiʻi's ecosystems (e.g., Aplet et al., 1998, Litton et al., 2006, Hughes et al., 2014, Blackmore and Vitousek, 2000).

Results presented here demonstrate the relative importance of sample plot density (i.e., the number of plots sampled across a given landscape of interest) over sample plot intensity (i.e., the degree to which different structural components are measured in a given inventory plot). When plot sample density was constrained to the standard FIA "1X" sampling regime (i.e., ca. 1 sample plot per 2400 ha), relative standard errors were, in most comparisons, 20% to 40% of mean values; such errors were high regardless of the degree of sampling intensity and clearly were not suitable for deriving ACD estimates at the landscape scale. In contrast, when plot density was maximized to include all 68 plots in the study, standard error values were 5% to 10% of mean values regardless of the degree of sampling intensity; such error values were well within suitability limits from which to derive ACD estimates at the landscape scale. It is worth noting that, regardless of sample intensity, standard error estimates collapsed to ca. 10% of mean values with the inclusion of 40 plots arrayed across Laupahoehoe and Puʻu Waʻawaʻa landscapes; this was the equivalent of 1 plot per 530 ha or an approximate "4X" FIA sampling regime. Collectively, results indicate that FIA inventory plots, even at their lowest sample intensity design, can be utilized in combination with LiDAR data to accurately estimate ACD across broad, heterogeneous landscapes, but only where plot densities are sufficiently high.

Prior studies have asserted the necessity of relatively large field plot dimensions (i.e., 0.5 to 1 ha) when linking forest plot data with LiDAR data to provide accurate estimates of ACD in tropical forests; analyses of such approaches found that ACD (or aboveground biomass) model errors declined with increasing sample plot size (Gobbakken and Naesset, 2009, Mascaro et al., 2011). Zolkos et al. (2013), and Asner and Mascaro (2014) posited that declines in relative error values with increasing sample plot size were caused by reduction in importance of edge effects in the co-located "footprints" of both field plots and LiDAR data coverage overlaying the field plot areas. These authors emphasized the need for highly accurate GPS locations for both plot and LiDAR footprints; they note that issues of misaligned or non-overlapping data coverages due to GPS inaccuracies are exacerbated when field plots and their associated LiDAR data coverages are relatively small. Our results demonstrated that this can be overcome at sufficiently high sample plot densities, and that FIA plot dimensions and configurations can be successfully employed to do so; relative standard errors approached 10% of mean ACD values at densities of one FIA plot per 530 ha even where small FIA "subplots dimensions" (i.e, 0.068 ha plot^{-1}) were employed. This result was surprising given prior findings regarding the need for sufficiently large plot size in such approaches (Zolkos et al., 2013, Mascaro et al., 2011). Results are promising regarding the utility of linking FIA plot data with LiDAR data to estimate ACD at landscape to regional-scales; the subplot design is the basic FIA sampling configuration, and it is the most commonly established and monitored FIA plot configuration and design throughout forested lands of the United States. As such, although FIA plot densities may need to be increased to make FIA plot/LiDAR approaches presented here viable, our results indicate that changes to plot sampling intensity does not appear necessary when utilizing FIA plots in combination with LiDAR to estimate ACD. Two factors may help to explain the low error values exhibited here. First, highly accurate survey grade GPS units were used to locate point center of all forest plots both on the ground and from the plane across Pu'u Wa'awa'a and Laupahoehoe landscapes; this is a necessity to any approach linking field plot data and LiDAR data to derive landscape ACD estimates (Mascaro et al., 2011). Second, vegetation of Laupahoehoe and Pu'u Wa'awa'a in particular, and Hawai'i in general, is lower stature and more homogenous with regard to tree species composition, and thus lidar allometrics, compared to more species rich tropical forests found elsewhere. Such characteristics may help to explain why smaller FIA plot dimensions may be acceptable, with regard to associated relative error values, for ACD estimation in Hawai'i's forests, but not necessarily for larger and/or more diverse forests of the continental tropics (Zolkos et al., 2013).

Notable among our results was the development and application of approaches to provide error estimates for landscape-scale ACD values. McRoberts (2010) posited that, given the enormous number of individual pixels involved, it was much too computationally intensive to determine variances of such data sets, and he offered a sampling approach whereby relevant N^2 terms (i.e, N being the number of pixels) are sampled within a systematic grid system overlaying given areas of interest. Results presented here indicate that the sampling approach offered by McRoberts (2010) is unnecessary and cumbersome. Rather, through application of straightforward algebraic techniques (Appendix A), we were able to readily provide an error estimate for the more than 100 million pixels that characterize the Laupahoehoe and Pu'u Wa'awa'a landscapes as well as any sub units of those landscapes (Appendix A); this error estimate was precisely the value McRoberts (2010) attempted to estimate via sampling. We assert that this approach can and should be employed in similar approaches where calculation of variance for thousands to millions of pixels is required.

Although costs of LiDAR data acquisition for large landscapes or regions may be high, the costs of increasing forest plot sampling density to levels that adequately capture the inherent heterogeneity of a given forested landscape in the absence of LiDAR data availability may be exorbitantly high as well; again, absent LiDAR data, our results demonstrated that plot densities would need to be doubled to tripled in number to approach relative error values exhibited by the field plot/LiDAR approaches. In some cases, increasing plot densities to suitable densities for accurate ACD estimates may not be feasible or even possible given topographic, accessibility, and/or safety constraints (Asner et al., 2011). As such, augmenting existing FIA forest plot data with region-specific LiDAR coverage, even if that requires an increase in plot density somewhat above the FIA standard 1X or 2X approaches, is a feasible, cost-effective, and scientifically sound approach from which to obtain accurate landscape- to regional-scale ACD measures from our nation's FIA network.

Acknowledgments

We sincerely thank K. Hiraoka, M. Murphy, and A. Cantan for their invaluable work collecting field data used in this study. We are also very grateful to S. Ayotte, D. Irvine, H. Hayden, M. Hansen, K.Thies, T. McGinely, R. Pattison, A. Lehman, C. Hubbard, R. Kolesar, G. Nicholas, J. Reid, T. Thompson, H. Anderson, A. Gray, and O. Kuegler for individual and collective efforts during all stages of Hawai'i Forest Inventory program funding, organization, training, data collection, data analysis, and data synthesis. Forest plot inventory fieldwork was supported by 2010 congressional appropriations dedicated to Forest Inventory and Analysis (FIA) intensification on USFS experimental forests; funds were administered by the Pacific Northwest Research Station – FIA program. We thank R. Ostertag for assistance in all aspects of local administration of funds as part of a cooperative agreement between USFS and the Research Corporation of the University of Hawai'i (RCUH); Ostertag also provided helpful comments on earlier versions of the manuscript. LiDAR data collection and processing were funded by the Avatar Alliance Foundation, Carnegie Institution for Science, and William R. Hearst IIII. LiDAR data analyses were supported by a Pacific Southwest Research Station, USDA-Forest Service internal grant award as well as the Carnegie Institution for Science. We thank the Hawai'i Island Branch of the Division of Forestry and Wildlife (DOFAW) and the Hawai'i Experimental Tropical Forest of the USDA-Forest Service (HETF) for permission to conduct field work on the Laupahoehoe and Laupahoehoe and Pu'u Wa'awa'a landscapes. The Carnegie Airborne Observatory has been made possible by grants and donations to G.P. Asner from the Ava-tar Alliance Foundation, Margaret A. Cargill Foundation, David and Lucile Packard Foundation, Gordon and Betty Moore Foundation, Grantham Foundation for the Protection of the Environment, W. M. Keck Foundation, John D. and Catherine T. MacArthur Foundation, Andrew Mellon Foundation, Mary Anne Nyburg Baker and G. Leonard Baker Jr, and William R. Hearst III. We thank R. Ostertag and two anonymous reviewers for providing helpful comments that improved earlier versions of the manuscript.

Appendix A

Here we develop the method for estimating the standard error of the area prediction without needing the subsampling described in McRoberts (2010). Essentially we apply some basic algebra to what McRoberts (2010) outlined to make the use of all N^2 covariance terms while still making the calculation feasible.

We first repeat some of the text to have all of the notation available in this appendix and the specific equations are generated. Then we describe the approach in general followed by how one could derived the variance formulas for a logistic regression from that general approach. Finally, we describe how we estimated the standard error for the original model but accounting for different LiDAR resolutions.

A.1. Estimating the standard error for the regression model

We used regression models to predict aboveground C mass per unit area (Mg/ha) and C mass for the entirety of both Laupahoehoe and Pu‘u Wa‘awa‘a landscapes; models determined the relationship between C mass estimates derived from FIA plots at discreet, known locations and mean LiDAR pixel heights that covered the same locations as each respective FIA forest plot ($n = 68$). Based on prior experience (Asner and Mascaro, 2014), we opted for an equation that allowed for increasing variability with increasing height in the following manner:

$$y = a\overline{ht}^{b} + \overline{ht}^{k}\varepsilon$$

where y is the estimated biomass per unit area in an FIA plot; $\overline{ht}$ is the mean height (i.e., TCH) from the associated pixels covering the given FIA plot; a, b, and k are constants to be estimated; and the residual error, ε, having a normal distribution with variance σ^2, (($\varepsilon \sim N(0, \sigma^2)$) (Asner and Mascaro, 2014).

The biomass estimate for any particular pixel where x is the associated TCH is constructed from estimates of a and b which are labeled as a and b: $\mu = ax^b$. Using the notation in McRoberts (2010) for the collection of N pixels in any given area of our overall study region in which we want to estimate aboveground C mass, we use a model-based estimate of mean C mass value per unit area (i.e., Mg/ha) calculated by the following:

$$\mu_{MOD} = \frac{1}{N}\sum_{i=1}^{N}\mu_i = \frac{1}{N}\sum_{i=1}^{N}ax_i^b$$

The coincident estimate of variance around the mean C mass was calculated by the following (McRoberts, 2010):

$$\widehat{\mathrm{Var}}(\mu_{MOD}) = \frac{1}{N^2}\sum_{i=1}^{N}\sum_{j=1}^{N}\widehat{\mathrm{Cov}}(\mu_i, \mu_j)$$

where $\widehat{\mathrm{Cov}}(\mu_i, \mu_j)$ is the estimate of the covariance between the two estimators, μ_i and μ_j.

McRoberts (2010) asserted that, because of the number of pixels involved, this estimate of variance is so computationally intensive as to require a sampling of a subset of the N^2 terms over an equidistant, two-dimensional grid superimposed over the respective area of interest. Sampling the data in this manner provides a means to make calculation of the variance estimate feasible (McRoberts, 2010).

However, we have determined that this approach is unnecessary. Again, following McRoberts (2010) we employed the Delta Method (Bishop et al., 1975) to approximate the covariance of functions of estimated parameters:

$$\widehat{\mathrm{Cov}}(\mu_i, \mu_j) = \widehat{\mathrm{Cov}}(ax_i^b, ax_j^b)$$

$$= \left(\frac{\partial ax_i^b}{\partial a}, \frac{\partial ax_i^b}{\partial b}\right)\Sigma_\beta\begin{pmatrix}\frac{\partial ax_j^b}{\partial a}\\ \frac{\partial ax_j^b}{\partial b}\end{pmatrix}$$

$$= (x_i^b, ax_i^b\log(x_i))\begin{pmatrix}\sigma_a^2 & \sigma_{a,b}\\ \sigma_{a,b} & \sigma_b^2\end{pmatrix}\begin{pmatrix}x_j^b\\ ax_j^b\log(x_j)\end{pmatrix}$$

$$= x_i^b x_j^b(\sigma_a^2 + a\sigma_{a,b}\log(x_j) + a\sigma_{a,b}\log(x_i) + a^2\sigma_b^2\log(x_i)\log(x_j))$$

where σ_a^2 and σ_b^2 are the respective estimates of variance for parameter estimates a and b, and $\sigma_{a,b}$ is the estimate of the covariance between a and b. We obtain an estimate of the covariance of two estimates from the estimated coefficients, the estimated variances, and the covariance of the estimators of a and b. All of these values are obtained from the regression output.

In summing over the N^2 combinations of pairs of pixels we note the following simplifications:

$$S^2 = \sum_{i=1}^{N}\sum_{j=1}^{N}x_i^b x_j^b = \left(\sum_{i=1}^{N}x_i^b\right)^2$$

$$S \times L = \sum_{i=1}^{N}\sum_{j=1}^{N}x_i^b x_j^b\log(x_j) = \left(\sum_{i=1}^{N}x_i^b\right)\left(\sum_{i=1}^{N}x_i^b\log(x_i)\right)$$

$$L^2 = \sum_{i=1}^{N}\sum_{j=1}^{N}x_i^b x_j^b\log(x_i)\log(x_j) = \left(\sum_{i=1}^{N}x_i^b\log(x_i)\right)\left(\sum_{i=1}^{N}x_i^b\log(x_i)\right)$$

Further, we let $x^b\log(x) \equiv 0$ when $x = 0$. This is a “natural” definition in that

$$\lim_{x\to 0^+}x^b\log(x) = 0$$

Consequently, we can express the estimate of variance for μ_{MOD} in the following manner:

$$\widehat{\mathrm{Var}}(\mu_{MOD}) = \frac{1}{N^2}(S^2\sigma_a^2 + 2SLa\sigma_{a,b}^2 + L^2a^2\sigma_b^2)$$

This expression does not require any sampling of the N^2 covariances. Rather, it provides an error estimate for both Pu‘u Wa‘awa‘a (ca. 72 million

1.5 m^2 pixels) and Laupahoehoe (ca. 32 million 1.25 m^2 pixels).

A.2. The general case

Considered more broadly, this approach to calculate the standard error of an estimated total can be generalized for any subset of the pixels and for any regression function. McRoberts (2010) uses an estimator of the following general form for an individual pixel:

$$\mu_i = f(X_i; \beta)$$

where β is a vector of estimated coefficients and X_i is a vector of covariates. The overall estimator for a collection of N pixels is the arithmetic average of all of those individual predictions:

$$\mu_{Mod} = \frac{1}{N}\sum_{i=1}^{N}\mu_i$$

As noted before the variance of μ_{Mod} is estimated with

$$\widehat{Var}(\mu_{Mod}) = \frac{1}{N^2}\sum_{i=1}^{N}\sum_{j=1}^{N}\widehat{Cov}(\mu_i, \mu_j)$$

McRoberts (2010) asserts that this double sum must be estimated by overlaying a grid to reduce the number of calculations to a computationally tractable amount. However, this grid sampling approach proves unnecessary in light of some basic algebra.

Following McRoberts (2010), we used the Delta Method (Bishop et al., 1975) to approximate (as opposed to calculate) $\widehat{Cov}(\mu_i, \mu_j)$. We first identified the vector of partial derivatives of μ_i with respect to each parameter:

$$Z_i = \left(\frac{\partial\mu_i}{\partial\beta_1}, \frac{\partial\mu_i}{\partial\beta_2}, ..., \frac{\partial\mu_i}{\partial\beta_J}\right)'$$

We then approximated $\widehat{Cov}(\mu_i, \mu_j)$ in the following manner:

$$\widehat{Cov}(\mu_i, \mu_j) \cong Z_i' V_\beta Z_j$$

$$= \sum_{k=1}^{J}\sum_{m=1}^{J}\frac{\partial\mu_i}{\partial\beta_k}\cdot\frac{\partial\mu_j}{\partial\beta_m}\cdot v_{km}$$

where v_{km} is the km-th element of V_β which is the estimated covariance matrix of the estimated coefficients.

Since the summation indices are not dependent on one another, we rearranged them without having to modify the indices:

$$\widehat{Var}(\mu_{Mod}) = \frac{1}{N^2}\sum_{k=1}^{J}\sum_{m=1}^{J}\sum_{i=1}^{N}\sum_{j=1}^{N}\frac{\partial\mu_i}{\partial\beta_k}\cdot\frac{\partial\mu_j}{\partial\beta_m}\cdot v_{km}$$

$$= \frac{1}{N^2}\sum_{k=1}^{J}\sum_{m=1}^{J}v_{km}\sum_{i=1}^{N}\frac{\partial\mu_i}{\partial\beta_k}\sum_{j=1}^{N}\frac{\partial\mu_j}{\partial\beta_m}$$

$$= \frac{1}{N^2}\sum_{k=1}^{J}\sum_{m=1}^{J}v_{km}T_k T_m$$

where

$$T_k = \sum_{i=1}^{N}\frac{\partial\mu_i}{\partial\beta_k}$$

This requires merely the sum of N terms for each of the T_1, T_2, ..., T_J statistics, a more direct task that requires far fewer computations than would be necessary to estimate the sum with N^2 terms. Further, this approach does not rely on an arbitrary sampling grid and provides an exact asymptotic variance rather than an approximate asymptotic variance (McRoberts, 2010).

For the specific example we considered earlier, we have $J = 2$, $v_{11} = \sigma_a^2$, $v_{22} = \sigma_b^2$, $v_{12} = v_{21} = \sigma_{a,b}$, $T_1 = S$, and $T_2 = L$.

A.3. A logistic regression example

McRoberts (2010) considered a logistic regression model with

$$\mu_i = 1-1/\left(1 + \exp\left(\sum_{k=1}^{J}\beta_k x_{ik}\right)\right)$$

predicting the proportion of pixels with a specific characteristic. Here we have $v_{kk} = \sigma_{\beta_k}^2$, $v_{km} = \sigma_{\beta_k,\beta_m}$ for $k \neq m$, and $T_k = \sum_{i=1}^{N} x_{ik}\mu_i(1-\mu_i)$.

A.4. Accounting for different LiDAR resolutions

Because LiDAR pixel resolutions differ for Laupahoehoe and Puu Waa Waa (i.e., 1.25 m^2 and 1.5 m^2, respectively), we cannot simply estimate the mean ($Mg\ ha^{-1}$) or total (Mg) C mass by weighting the number of pixels in each area. Instead, it is more appropriate to estimate the mean as a weighted mean in which the weights are the areas of the two regions. As such, we expressed A_{Lau} and A_{Puu} to indicate the two areas, and used μ_{Lau} and μ_{Puu} to indicate mean C mass ha^{-1}; the weighted mean C mass ha^{-1} of the combined area is expressed as:

$$\mu = w_{Lau}\mu_{Lau} + w_{Puu}\mu_{Puu}$$

where $w_{Lau} = \frac{A_{Lau}}{A_{Lau}+A_{Puu}}$ and $w_{Puu} = \frac{A_{Puu}}{A_{Lau}+A_{Puu}}$.

The estimated variance of μ is somewhat more complicated, and it is expressed in the following manner:

$$\sigma_\mu^2 = \frac{w_{Lau}^2}{N_{Lau}^2}\sum_{i=1}^{N_{Lau}}\sum_{j=1}^{N_{Lau}} Cov(ax_i^b, ax_j^b) + \frac{w_{Puu}^2}{N_{Puu}^2}\sum_{i=1}^{N_{Puu}}\sum_{j=1}^{N_{Puu}} Cov(ay_i^b, ay_j^b) + \frac{2w_{Lau}w_{Puu}}{N_{Lau}N_{Puu}}\sum_{i=1}^{N_{Lau}}\sum_{j=1}^{N_{Puu}} Cov(ax_i^b, ay_j^b)$$
$$= v_{Lau} + v_{Puu} + v_{L\times P}.$$

We have previously demonstrated the following:

Consequently, we simply solve for each of the three terms above:

$$v_{Lau} = \frac{w_{Lau}^2}{N_{Lau}^2}\sum_{i=1}^{N_{Lau}}\sum_{j=1}^{N_{Lau}} Cov(ax_i^b, ax_j^b)$$

$$= \frac{w_{Lau}^2}{N_{Lau}^2}\sum_{i=1}^{N_{Lau}}\sum_{j=1}^{N_{Lau}} x_i^b x_j^b(\sigma_a^2 + a\sigma_{a,b}\log(x_j) + a\sigma_{a,b}\log(x_i) + a^2\sigma_b^2\log(x_i)\log(x_j))$$

$$= \frac{w_{Lau}^2}{N_{Lau}^2}\left(\sigma_a^2\left(\sum_{i=1}^{N_{Lau}} x_i^b\right)^2 + 2a\sigma_{a,b}\left(\sum_{i=1}^{N_{Lau}} x_i^b\right)\left(\sum_{i=1}^{N_{Lau}} x_i^b\log(x_i)\right) + a^2\sigma_b^2\left(\sum_{i=1}^{N_{Lau}} x_i^b\log(x_i)\right)^2\right)$$

$$v_{Puu} = \frac{w_{Puu}^2}{N_{Puu}^2}\left(\sigma_a^2\left(\sum_{i=1}^{N_{Puu}} y_i^b\right)^2 + 2a\sigma_{a,b}\left(\sum_{i=1}^{N_{Puu}} y_i^b\right)\left(\sum_{i=1}^{N_{Puu}} y_i^b\log(y_i)\right) + a^2\sigma_b^2\left(\sum_{i=1}^{N_{Puu}} y_i^b\log(y_i)\right)^2\right)$$

$$v_{L\times P} = \frac{2w_{Lau}w_{Puu}}{N_{Lau}N_{Puu}}\sum_{i=1}^{N_{Lau}}\sum_{j=1}^{N_{Puu}} Cov(ax_i^b, ay_j^b)$$

$$= \frac{2w_{Lau}w_{Puu}}{N_{Lau}N_{Puu}}\sum_{i=1}^{N_{Lau}}\sum_{j=1}^{N_{Puu}} x_i^b y_j^b(\sigma_a^2 + a\sigma_{a,b}\log(y_j) + a\sigma_{a,b}\log(x_i) + a^2\sigma_b^2\log(x_i)\log(y_j))$$

$$= \frac{2w_{Lau}w_{Puu}}{N_{Lau}N_{Puu}}\left(\sigma_a^2\left(\sum_{i=1}^{N_{Lau}} x_i^b\right)\left(\sum_{j=1}^{N_{Puu}} y_j^b\right) + a\sigma_{a,b}\left(\sum_{i=1}^{N_{Lau}} x_i^b\right)\left(\sum_{j=1}^{N_{Puu}} y_j^b\log(y_j)\right) + a\sigma_{a,b}\left(\sum_{i=1}^{N_{Lau}} x_i^b\log(x_i)\right)\left(\sum_{j=1}^{N_{Puu}} y_j^b\right)\right.$$
$$\left. + a^2\sigma_b^2\left(\sum_{i=1}^{N_{Lau}} x_i^b\log(x_i)\right)\left(\sum_{j=1}^{N_{Puu}} y_j^b\log(y_j)\right)\right)$$

Appendix B. Supplementary material

Supplementary data associated with this article can be found, in the online version, at https://doi.org/10.1016/j.foreco.2018.04.053.

References

Alvarez-Davila, E., Cayuela, L., Gonzalez-Caro, S., Aldana, A.M., Stevenson, P.R., Phillips, O., Cogollo, A., Penuela, M.C., von Hildebrand, P., Jimenez, E., Melo, O., Londono-Vega, A.C., Mendoza, I., Velasquez, O., Fernandez, F., Serna, M., Velazquez-Rua, C., Benitez, D., Rey-Benayas, J.A.M., 2017. Forest biomass density across large climate gradients in northern South America is related to water availability but not with temperature. Plos One 12. http://dx.doi.org/10.1371/journal.pone.0171072.

Aplet, G.H., Hughes, R.F., Vitousek, P.M., 1998. Ecosystem development on Hawaiian lava flows: biomass and species composition. J. Veg. Sci. 9, 17–26.

Asner, G.P., Hughes, R.F., Varga, T.A., Knapp, D.E., Kennedy-Bowdoin, T., 2009. Environmental and biotic controls over aboveground biomass throughout a tropical rain forest. Ecosystems. http://dx.doi.org/10.1007/s10021-008-9221-5.

Asner, G.P., Powell, G.V.N., Mascaro, J., Knapp, D.E., Clark, J.K., Jacobson, J., Kennedy-Bowdoin, T., Balaji, A., Paez-Acosta, G., Victoria, E., Secada, L., Valqui, M., Hughes, R.F., 2010. High-resolution forest carbon stocks and emissions in the Amazon. Proc. Nat. Acad. Sci. USA 107, 16738–16742.

Asner, G.P., Hughes, R.F., Mascaro, J., Uowolo, A.L., Knapp, D.E., Jacobson, J., Kennedy-Bowdoin, T., Clark, J.K., 2011. High-resolution carbon mapping on the million-hectare Island of Hawaii. Front. Ecol. Environ. 9 (8), 434–439.

Asner, G.P., Mascaro, J., Muller-Landau, H.C., Vieilledent, G., Vaudry, R., Rasamoelina, M., Hall, J.S., van Breugel, M., 2012a. A universal airborne LiDAR approach for tropical forest carbon mapping. Biotropica 168, 1147–1160.

Asner, G.P., Clark, J.K., Mascaro, J., Garcia, G.A.G., Chadwick, K.D., Encinales, D.A.N., Paez-Acosta, G., Montenegro, E.C., Kennedy-Bowdoin, T., Duque, A., Balaji, A., von Hildebrand, P., Maatoug, L., Bernal, J.F.P., Quintero, A.P.Y., Knapp, D.E., Davila, M.C.G., Jacobson, J., Ordonez, M.F., 2012b. High-resolution mapping of forest carbon stocks in the Colombian Amazon. Biogeosciences 9 (7), 2683–2696.

Asner, G.P., Mascaro, J., 2014. Mapping tropical forest carbon: Calibrating plot estimates to a simple LiDAR metric. Remote Sens. Environ. 140, 614–624.

Asner, G.P., Sousan, S., Knapp, D.E., Selmants, P.C., Martin, R.E., Hughes, R.F., Giardina, C.P., 2016. Rapid forest carbon assessments of oceanic islands: a case study of the Hawaiian archipelago. Carbon Balance Manage. 11, 1. http://dx.doi.org/10.1186/s13021-015-0043-4.

Bechtold, W.A., Patterson, P.L., 2005. The enhanced forest inventory and analysis program - national sampling design and estimation procedures. Gen. Tech. Rep. SRS-80. Asheville, NC: U.S. Department of Agriculture, Forest Service, Southern Research Station. 85 p.

Belote, R.T., Aplet, G.H., 2014. Land protection and timber harvesting along productivity and diversity gradients in the Northern Rocky Mountains. Ecosphere 5, 1–19.

Bishop, Y.M.M., Fienberg, S.E., Holland, P.W., 1975. Discrete Multivariate Analysis. Massachusetts Institute of Technology Press, Cambridge.

Blackard, J.A., Finco, M.V., Helmer, E.H., Holden, G.R., Hoppus, M.L., Jacobs, D.M., Lister, A.J., Moisen, G.G., Nelson, M.D., Riemann, R., Ruefenacht, B., Salajanu, D., Weyermann, D.L., Winterberger, K.C., Brandeis, T.J., Czaplewski, R.L., McRoberts, R.E., Patterson, P.L., Tymcio, R.P., 2008. Mapping US forest biomass using nation-wide forest inventory data and moderate resolution information. Remote Sens. Environ. 112, 1658–1677.

Blackmore, M., Vitousek, P.M., 2000. Cattle grazing, forest loss, and fuel loading in a dry forest ecosystem at Pu'u Wa'aWa'a ranch, Hawai'i. Biotropica 32, 625–632.

Cairns, M.A., Brown, S., Helmer, E.H., Baumgardner, G.A., 1997. Root biomass allocation in the world's upland forests. Oecologia 111, 1–11.

Canadell, J.G., Le Quéré, C., Raupach, M.R., Field, C.B., Buitenhuis, E.T., Ciais, P., Conway, T.J., Gillett, N.P., Houghton, R.A., Marland, G., 2007. Contributions to accelerating atmospheric CO2 growth from economic activity, carbon intensity, and efficiency of natural sinks. PNAS 104, 18866–18870.
Chave, J., Condit, R., Aguilar, S., Hernandez, A., Lao, S., Perez, R., 2004. Error propagation and scaling for tropical forest biomass estimates. Philosophical Trans. Roy. Soc. London Series B – Biol. Sci. 359, 409–420.
Chave, J., Andalo, C., Brown, S., Cairns, M.A., Chambers, J.Q., Eamus, D., Fölster, H., Fromard, F., Higuchi, T.K., Lescure, J.P., Nelson, B.W., Ogawa, H., Puig, H., Riéra, B., Yamakura, T., 2005. Tree allometry and improved estimation of carbon stocks and balance in tropical forests. Oecologia 145, 87–99.
Chopping, M., Schaaf, C.B., Zhao, F., Wang, Z.S., Nolin, A.W., Moisen, G.G., Martonchik, J.V., Bull, M., 2011. Forest structure and aboveground biomass in the southwestern United States from MODIS and MISR. Remote Sens. Environ. 115, 2943–2953.
Cuddihy, L.W., Stone, C.P., 1990. Alteration of native Hawaiian vegetation: effects of humans, their activities and introductions. University of Hawai'i Press, Honolulu, Hawai'i, USA.
Desprez, J., Iannone III, B.V., Yang, P., Oswalt, C.M., Fei, S.L., 2014. Northward migration under a changing climate: a case study of blackgum (Nyssa sylvatica). Clim. Change 126, 151–162.
Domke, G.M., Woodall, C.W., Walters, B.F., McRoberts, R.E., Hatfield, M.A., 2014. Strategies to compensate for the effects of nonresponse on forest carbon baseline estimates from the national forest inventory of the United States. For. Ecol. Manage. 315, 112–120.
Drake, J.B., Dubayah, R.O., Clark, D.B., Knox, R.G., Blair, J.B., Hofton, M.A., Chazdon, R.L., Weishampel, J.F., Prince, S.D., 2002. Estimation of tropical forest structural characteristics using large-footprint lidar. Remote Sens. Environ. 79, 305–319.
Dudley, B.D., Hughes, R.F., Ostertag, R., 2014. Groundwater availability mediates the ecosystem effects of an invasion of Prosopis pallida. Ecol. Appl. 24, 1954–1971.
Efron, B., 1982. The jackknife, the bootstrap, and other resampling plans 38. Society of Industrial and Applied Mathematics CBMS-NSF Monographs. ISBN 0-89871-179-7.
Giambelluca, T.W., Chen, Q., Frazier, A.G., Price, J.P., Chen, Y.-L., Chu, P.-S., Eischeid, J.K., Delparte, D.M., 2013. Online Rainfall Atlas of Hawai'i. Bull. Amer. Meteor. Soc. 94, 313–316. http://dx.doi.org/10.1175/BAMS-D-11-00228.1.
Gibson, R.K., Bradstock, R.A., Penman, T.D., Keith, D.A., Driscoll, D.A., 2014. Changing dominance of key plant species across a Mediterranean climate region: implications for fuel types and future fire regimes. Plant Ecol. 215, 83–95.
Gobakken, T., Naesset, E., 2009. Assessing effects of positioning errors and sample plot size on biophysical stand properties derived from airborne laser scanner data. Can. J. For. Res. 39, 1036–1052.
Gon, S.M., Allison, A., Cannarella, R.J., Jacobi, J.D., Kaneshiro, K.Y., Kido, M.H., et al., 2006. A GAP analysis of Hawai'i: Final report. US Department of the Interior. US Geological Survey, Washington, DC.
Gray, A.N., Whittier, T.R., 2014. Carbon stocks and changes on Pacific Northwest national forests and the role of disturbance, management, and growth. For. Ecol. Manage. 328, 167–178.
Haavik, L.J., Coleman, T.W., Flint, M.L., Venette, R.C., 2012. Agrilus auroguttatus exit hole distributions on Quercus agrifolia boles and a sampling method to estimate their density on individual trees. Can. Entomol. 144, 767–778.
Houghton, R.A., Hall, F., Goetz1, S.J., 2009. Importance of biomass in the global carbon cycle. J. Geophys. Res. 114. http://dx.doi.org/10.1029/2009JG000935.
Huebner, C.D., Morin, R.S., Zurbriggen, A., White, R.L., Moore, A., Twardus, D., 2009. Patterns of exotic plant invasions in Pennsylvania's Allegheny National Forest using intensive Forest Inventory and Analysis plots. For. Ecol. Manage. 257, 258–270.
Hughes, R.F., Asner, G.P., Mascaro, J., Uowolo, A., Baldwin, J., 2014. Carbon storage landscapes of lowland Hawai'i: the role of native and invasive species through space and time. Ecol. Appl. 24, 716–731.
Kellndorfer, J.M., Walker, W.S., LaPoint, E., Kirsch, K., Bishop, J., Fiske, G., 2010. Statistical fusion of lidar, InSAR, and optical remote sensing data for forest stand height characterization: A regional-scale method based on LVIS, SRTM, Landsat ETM plus, and ancillary data sets. J. Geophys. Res.-Biogeosci. 115, 1–10.
Lefsky, M.A., Harding, D., Cohen, W., Parker, G., Shugart, H., 1999. Surface lidar remote sensing of basal area and biomass in deciduous forests of eastern Maryland, USA. Remote Sens. Environ. 67, 83–98.
Lefsky, M.A., Cohen, W.B., Harding, D.J., Parker, G.G., Acker, S.A., Gower, S.T., 2002. Lidar remote sensing of above-ground biomass in three biomes. Glob. Ecol. Biogeogr. 11, 393–399.
Leopold, C.R., Hess, S.C., 2017. Conversion of native terrestrial ecosystems in Hawai'i to novel grazing systems: a review. Biol. Invasions 19, 161–177.
Litton, C.M., Sandquist, D.R., Cordell, S., 2006. Effects of non-native grass invasion on aboveground carbon pools and tree population structure in a tropical dry forest of Hawai'i. For. Ecol. Manage. 231, 105–113.
Mascaro, J., Asner, G.P., Muller-Landau, H.C., van Breugel, M., Hall, J., Dahlin, K., 2011. Controls over aboveground forest carbon density on Barro Colorado Island, Panama. Biogeosciences 8, 1615–1629.
McRoberts, R.E., 2010. Probability- and model-based approaches to inference for proportion forest using satellite imagery as ancillary data. Remote Sens. Environ. 114, 1017–1025.
McRoberts, R.E., Naesset, E., Gobakken, T., Bollandsas, O.M., 2015. Indirect and direct estimation of forest biomass change using forest inventory and airborne laser scanning data. Remote Sens. Environ. 164, 36–42.
Mehta, N., Pandya, N.R., Thomas, V.O., Krishnayya, N.S.R., 2014. Impact of rainfall gradient on aboveground biomass and soil organic carbon dynamics of forest covers in Gujarat, India. Ecol. Res. 29, 1053–1063.
Navar, J., 2009. Allometric equations for tree species and carbon stocks for forests of northwestern Mexico. For. Ecol. Manage. 257, 427–434.
Saatchi, S.S., Houghton, R.A., Alvala, R.C.D.S., Soares, J.V., Yu, Y., 2007. Distribution of aboveground live biomass in the Amazon basin. Glob. Change Biol. 13, 816–837.
Sanderson, M., 1993. Prevailing trade winds: Weather and climate in Hawai'i. University of Hawai'i Press, Honolulu, Hawai'i, USA.
Skowronski, N., Clark, K., Nelson, R., Hom, J., Patterson, M., 2007. Remotely sensed measurements of forest structure and fuel loads in the Pinelands of New Jersey. Remote Sens. Environ. 108, 123–129.
Swetnam, T.L., Brooks, P.D., Barnard, H.R., Harpold, A.A., Gallo, E.L., 2017. Topographically driven differences in energy and water constrain climatic control on forest carbon sequestration. Ecosphere 8. http://dx.doi.org/10.1002/ecs2.1797.
Thompson, M.T., 2009. Analysis of conifer mortality in Colorado using forest inventory and analysis's annual forest inventory. West. J. Appl. For. 24, 193–197.
Trauernicht, C., Pickett, E., Giardina, C.P., Litton, C.M., Cordell, S., Beavers, A., 2015. The contemporary scale and context of wildfire in Hawai'i. Pac. Sci. 69, 427–444.
US ENVIRONMENTAL PROTECTION AGENCY, 2011. Inventory of US greenhouse gas emissions and sinks: 1990–2010. EPA 430-R-12-001. Available online, www.epa.gov/climatechange/emissions/usinventoryreport. html; last accessed Dec. 10, 2012.
UN REDD PROGRAMME, 2012. Available online at www.un-redd.org/; last accessed May 29, 2012.
Wagner, W.L., Herbst, D.R., Sohmer, S.H., 1999. Manual of the flowering plants of Hawai'i. University of Hawai'i Press, Honolulu, Hawai'i, USA.
Walker, W.S., Kellndorfer, J.M., LaPoint, E., Hoppus, M., Westfall, J., 2007. An empirical InSAR-optical fusion approach to mapping vegetation canopy height. Remote Sens. Environ. 109, 482–499.
Wang, H.-H., Grant, W.E., Swannack, T.M., Gan, J., Rogers, W.E., Koralewski, T.E., Miller, J.H., Taylor, J.W., 2011. Predicted range expansion of Chinese tallow tree (Triadica sebifera) in forestlands of the southern United States. Divers. Distrib. 17, 552–565.
Waring, R.H., Coops, N.C., Mathys, A., Hilker, T., Latta, G., 2014. Process-based modeling to assess the effects of recent climatic variation on site Productivity and forest function across Western North America. Forests 5, 518–534.
Wolfe, E.W., Morris, J., 1996. Geologic Map of the Island of Hawaii; Map I-2524-A. Miscellaneous Investigations Series; U.S. Geological Survey.
Woodcock, D., 2003. To restore the watersheds: Early twentieth century tree planting in Hawai'i. Ann. Assoc. Am. Geogr. 93, 624–635.
Zhao, Feng, Guo, Qinghua, Kelly, Maggi, 2012. Allometric equation choice impacts lidar-based forest biomass estimates: A case study from the Sierra National Forest, CA. Agric. For. Meteorol. 165, 64–72.
Zimmerman, N., Hughes, R.F., Cordell, S., Hart, P., Chang, H.K., Perez, D., Like, R.K., Ostertag, R., 2008. Patterns of primary succession of native and introduced plants in lowland wet forests in eastern Hawai'i. Biotropica 40, 277–284.
Zolkos, S.G., Goetz, S.J., Dubayah, R., 2013. A meta-analysis of terrestrial aboveground biomass estimation using lidar remote sensing. Remote Sens. Environ. 128, 289–298.